AD-A256 674

PL-TR-92-2026

BASIC RESEARCH IN THE MEASUREMENT, ANALYSIS, AND MODELING OF ATMOSPHERIC EMISSIONS

J. W. Carpenter   M. E. Gardner
C. J. Beeler   C. H. Humphrey
T. M. Codella   R. J. Rieder
G. E. Galica   O. Shepherd

Visidyne, Inc
10 Corporate Place
South Bedford Street
Burlington, MA 01803

DTIC
ELECTE
OCT 01 1992
S A D

December 1991

Scientific Report No. 1

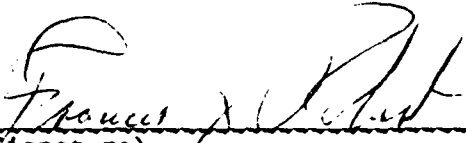APPROVED FOR PUBLIC RELEASE; DISTRIBUTION UNLIMITED
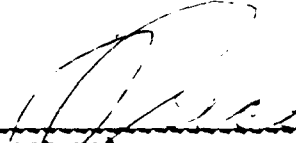
92 9 30 020

92-26205

PHILLIPS LABORATORY
AIR FORCE SYSTEMS COMMAND
HANSCOM AIR FORCE BASE, MASSACHUSETTS 01731-5000

This technical report has been reviewed and is approved for publication.

(Signature)

(Signature)
FRANCIS X. ROBERT
Contract Manager

(Signature)
STEPHAN PRICE
Branch Chief

(Signature)
ALAN BLACKBURN, Lt Col, USAF
Division Director

This document has been reviewed by the ESD Public Affairs Office (PA) and is releasable to the National Technical Information Service (NTIS).

Qualified requestors may obtain additional copies from the Defense Technical Information Center. All others should apply to the National Technical Information Service.

REPORT DOCUMENTATION PAGE

Public reporting burden for this collection of information is estimated to average 1 hour per response, including the time for reviewing instructions, searching existing data sources, gathering and maintaining the data needed, and completing and reviewing the collection of information. Send comments regarding this burden estimate or any other aspect of this collection of information, including suggestions for reducing this burden, to Washington Headquarters Services, Directorate for Information Operations and Reports, 1215 Jefferson Davis Highway, Suite 1204, Arlington, VA 22202-4302, and to the Office of Management and Budget, Paperwork Reduction Project (0704-0188), Washington, DC 20503.

1. AGENCY USE ONLY (Leave blank)	2. REPORT DATE	3. REPORT TYPE AND DATES COVERED
	December 1991	Scientific No. 1

4. TITLE AND SUBTITLE

Basic Research in the Measurement, Analysis, and Modeling of Atmospheric Emissions

5. FUNDING NUMBERS

PE 632206
PR 5321 TA06 WUAB

F19628-90-C-0187

6. AUTHOR(S)

J.W. Carpenter, C.J. Beeler, T.M. Codella, G.E. Galica, M.E. Gardner, C.H. Humphrey, R.J. Rieder, O. Shepherd

7. PERFORMING ORGANIZATION NAME(S) AND ADDRESS(ES)

Visidyne, Inc.
10 Corporate Place
South Bedford Street
Burlington, MA 01803

8. PERFORMING ORGANIZATION REPORT NUMBER

VI-1798

9. SPONSORING/MONITORING AGENCY NAME(S) AND ADDRESS(ES)

Phillips Laboratory
Hanscom AFB, MA 01731-5000

Contract Manager: Frank Robert, GPOB

10. SPONSORING/MONITORING AGENCY REPORT NUMBER

PL-TR-92-2026

11. SUPPLEMENTARY NOTES

12a. DISTRIBUTION/AVAILABILITY STATEMENT

Approved for public release; distribution unlimited

12b. DISTRIBUTION CODE

13. ABSTRACT (Maximum 200 words)

This interim scientific report covers the work accomplished during the first fiscal year of Contract F19628-90-C-0187. The objectives of this contract are to perform basic research in several areas related to optical and infrared systems technology. The areas receiving funcing during the first fiscal year included the following:
1. Modeling of High Temperature Molecular Data
2. Cloud Background Measurement, Analysis, and Modeling
3. High Altitude Atmospheric Emissions
4. Analysis of Satellite Data

Work in these areas included modeling CO_2 and H_2O emissions, supporting the Infrared Background Signature Survey (IBSS), providing the CIRRIS 1A experiment with a variety of task supports, designing earthlimb radiance structure measurement experiments for the MSX flights, modeling high altitude water emissions, and analyzing spectral, spatial, temporal data from some of the instrumentation provided by Visisydne for the EXCEDE III atmospheric energy deposition experiment.

14. SUBJECT TERMS

Atmospheric molecular emissions
Earthlimb radiance structure
Analysis of rocket and satellite data
Cloud backgrounds
Ambient-spacecraft interactions

15. NUMBER OF PAGES

74

16. PRICE CODE

17. SECURITY CLASSIFICATION OF REPORT	18. SECURITY CLASSIFICATION OF THIS PAGE	19. SECURITY CLASSIFICATION OF ABSTRACT	20. LIMITATION OF ABSTRACT
UNCLASSIFIED	UNCLASSIFIED	UNCLASSIFIED	SAR

NSN 7540-01-280-5500

Standard Form 298 (Rev 2-89)
Prescribed by ANSI Std. Z39-18
298-102

TABLE OF CONTENTS

TABLE OF CONTENTS

LIST OF FIGURES

LIST OF TABLES

1.0 INTRODUCTION

This interim scientific report covers the work undertaken for the period 26 September 1990 through 30 September 1991 on contract F19628-90-C-0187. This was the first year of a three year contract. The effort was in the area of basic research in the measurement, analysis, and modeling of atmospheric emission processes. Section 2 of this report covers the theoretical studies to provide improved modeling of high temperature molecular emissions. Cloud background modeling based on analysis of satellite data, including IBSS, is discussed in Section 3. Section 4 describes support for the CIRRIS 1A instrument operations. A discussion of the MSX earthlimb background experiments is included in Section 5. The effort in modeling and measurement of high altitude water vapor emissions is presented in Section 6. The initial analysis of high altitude atmospheric emissions at high dosing levels is covered in Section 7.

2.0 MODELING OF HIGH TEMPERATURE MOLECULAR PHYSICS

In this first year of the contract, two molecules were studies and calculated, CO_2 and H_2O. A new HITRAN database will be available in early 1992. The previous version of this database utilized direct numerical diagnolization (DND) calculations for all unobserved $^{12}C^{16}O_2$ parallel band intensities. The new database will utilize DND calculations for all unobserved lines of the three most abundant isotopic species: $^{12}C^{16}O_2$, $^{13}C^{16}O_2$, and $^{16}O^{12}C^{18}O$. This new DND data have required the generation of Herman-Wallis parameters (which include the effects of rotation-vibration on line intensity) and an important extension to the DND technique: the calculation of molecular properties for the asymmetric linear molecule. A very complicated transform of both the potential and the dipole moment functions was required for these new calculations which included many thousands of terms. DND line position information has also been employed where observed line positions are not available. The semifinal generation of the band and line parameters has been concluded, and more importantly, validation of the parameters for HITRAN purposes has been started.

A considerable part of the current effort has been spent on the reformulation of the DND technique to handle bent triatomic molecules and to better treat higher temperature calculations. To this end, software from Rice University has been utilized for the basis functions, a kinetic

1

energy operator developed by an English team has been used, and a potential function calculated by a German researcher has been employed. The calculation of vibrational levels indicates that accuracies of several cm^{-1} are achievable at present.

3.0 IBSS EXPERIMENT DATA SUPPORT

3.1 Introduction

Visidyne supported the Infrared Background Signature Survey (IBSS). These phenomena are relevant to Strategic Defense Initiative Organization (SDIO) and the Global Protection Against Limited Strike (GPALS) system concept. They include earth and earthlimb backgrounds, plumes that represent missile signatures, missile fuel observables, and other phenomena.

The mission was accomplished through use of a cryogenically cooled infrared spectrometer and radiometer (IR Sensor), an ultraviolet, visible, and near infrared spectrograph/imager (Arizona Imager/Spectrograph (AIS)), a pair of low light level television (L^{3}TV) cameras, and additional instrumentation mounted on the improved Shuttle Pallet Satellite platform (SPAS II). The combined fields of view of all SPAS-mounted instrumentation are shown in Fig. 1. The spacecraft was deployed from the cargo bay by the Remote Manipulator System (RMS), and the Orbiter then maneuvered from the vicinity. Multispectral measurements encompassing the UV, visible, and IR regions of the spectrum were taken of plumes from Orbiter engine firings, the earthlimb, the hard earth, the Orbiter environment, chemical and gas releases, and calibration sources. Additional measurements were made while the SPAS II was berthed in the cargo bay or grappled by the RMS.

Space-based IR surveillance sensors, such as Brilliant Eyes, viewing above-the-horizon have three major sources of radiation which limit or impact their observing capabilities-celestial sources, zodiacal radiance, and the earthlimb radiance which varies in intensity and wavelength according to altitude, time of day, geographic location and geomagnetic conditions. The IBSS measurement will contribute to the understanding of IR spatial and spectral characteristics of the earthlimb background by observing the earthlimb at a variety of tangent altitudes and through a variety of radiometric filters. In addition, selected measurements were made viewing below-

FOV DIMENSIONS

	YAW (deg)	PITCH (deg)
AIS WIR	17.0	19.3
AIS MVIS	4.8	5.4
AIS SPECTROMETER	0.1	2.0
AIS WUV	24.1	27.0
AIS NUV & NIR	1.8	2.1
L3TV WFOV	14.7	11.00
L3TV NFOV	4.9	3.6
IR RADIOMETER LINE ARRAY	0.6394	0.20
SCANNED IR RADIOMETER	0.6394	9.626
IR SPECTROMETER	1.03	0.0607
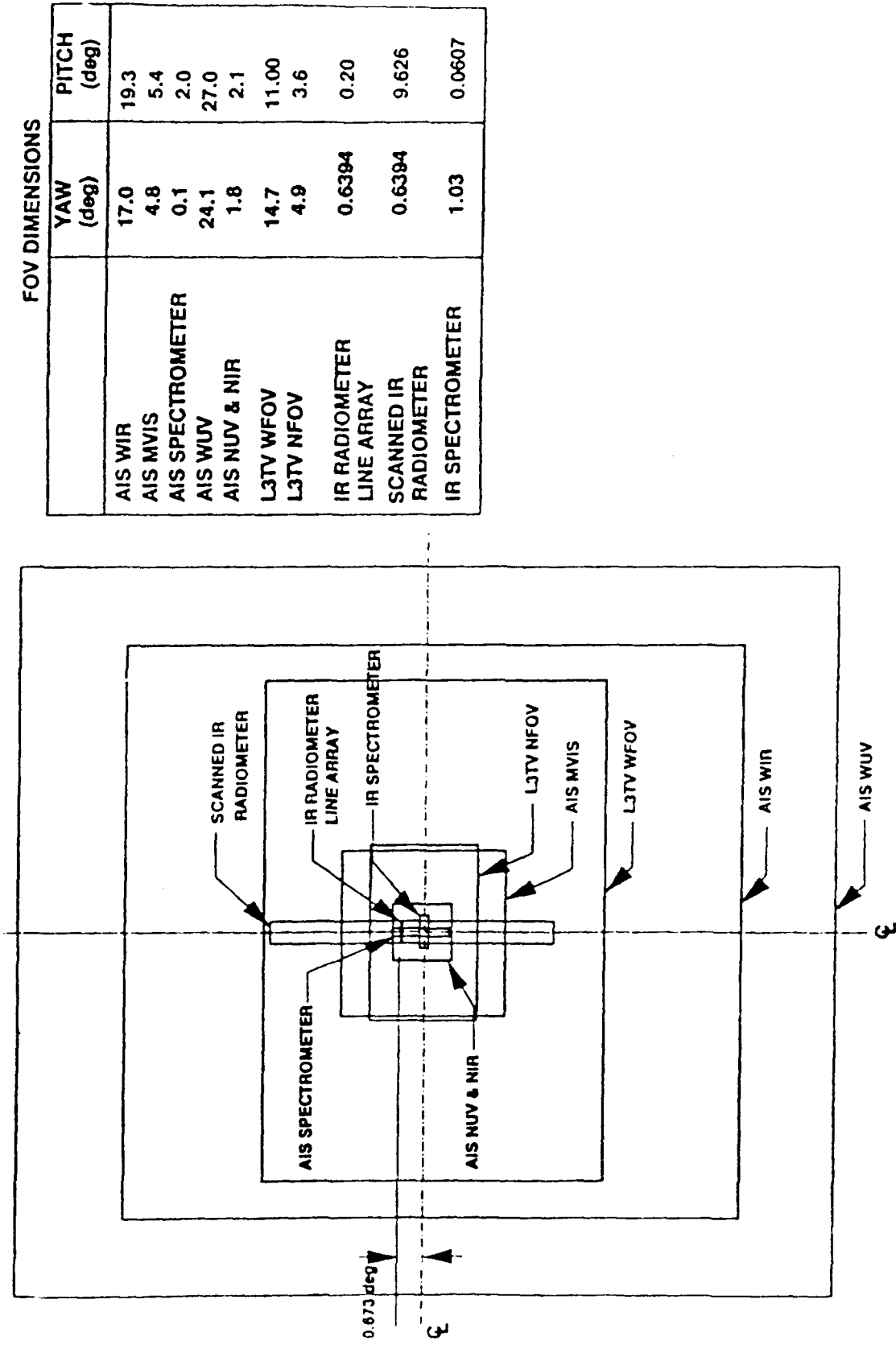
Figure 1. Combined IBSS Instrument Fields of View

3

the-horizon (earthscan mode). The down-looking, hard earth measurements are intended to quantify the complex radiation transfer emissions of carbon dioxide. This information, coupled with the earthlimb measurements, form a continuous set of required measurements to adequately model the atmospheric infrared emissions from the earth background. The Brilliant Pebbles concept and other system will encounter these types of backgrounds.

3.2 Experiment Planning and Support

Initial efforts performed by Visidyne were in the area of analysis of the calibration data supplied by Utah State and from the measurements performed at the Kennedy Space Center. The results of this effort by C.J. Beeler of Visidyne are presented in GL Technical Memorandum No. 19, entitled, "Analysis of IBSS Radiometer Test Data" written in conjunction with W.F. Grieder of Grieder Research Engineering and D.S. Avtgis and H.T. Wadzinski of Boston College. Visidyne directly supported the earth background principal investigator during the Shuttle flights. This effort consisted of technical support, within the POCC, as well as off-site quick look analysis to assist in experiment replanning and quick look reporting.

In preparation for this support during the last week in January (January 29-31) Visidyne participated in a long duration Joint Integrated Simulation (JIS) to prepare for flight operations of the Shuttle flight. The STS-39 flight was originally planned for launch on March 9, 1991 but was postponed in early March until April 26, 1991.

To support this effort, a program was written which determined the orbital elements, semimajor axis, eccentricity, inclination, longitude of the ascending node, argument of perigee, and true and mean anomaly from state vectors. Given the orbital elements as input, Visidyne developed a program which tracked the orbit of the SPAS. From this program, the latitude, longitude, and height of the SPAS are determined. Visidyne generated a program which calculates the location of a specular point relative to a shuttle position. If yaw, pitch, and roll data are made available, Visidyne can determine the actual azimuth and elevation of the Shuttle and compute the earth centered angle between the actual specular point and the point where the Shuttle is looking.

Efforts also continued in the analysis of the calibration data from measurements performed at the Kennedy Space Center.

The Shuttle Discovery STS-39 was launched on April 28, 1991 at 0733:13.98 Eastern Daylight Time (GMT: 118:11:33:14) from Kennedy Space Center. The Discovery cargo consisted primarily of CIRRIS 1A and IBSS. Approximately 41 minutes after launch the orbiter was inserted into a nearly circular orbit of approximately 138 nautical miles with an inclination of approximately 57°. The SPAS was deployed from the orbiter at MET 2 day, 20 hours, 44 minutes (orbiter revolution 47).

During the SPAS operations, both deployed and RMS 22 measurement blocks were made of the solar specular region, hard earth, earthlimb, and aurora. All major backgrounds experimental objectives were achieved. Extensive measurements were made of the CO_2 backgrounds in earth scan, and both horizontal and vertical earthlimb modes. Additional measurements were made throughout the SWIR and MWIR spectral regions (2.3 - 7.7 μm) in both the earthlimb and hard earth modes.

The first earthlimb measurement began during revolution 36 at MET 2 days, 4 hours, 13 minutes. The earthlimb observations consisted of a series of measurement sets in which the earthlimb was scanned in the pushbroom mode by the orbital motion of the SPAS while the IR sensor was viewing approximately 100° off-track. The filter wheel cycled through the seven different spectral filters and the internal calibration source for a range of tangent altitudes. The measurements included day, night and terminator conditions.

The most stressing region of the natural background is thought to be in the vicinity of the solar specular point. It is for this reason that the primary objective of the IBSS earth backgrounds experiment was measurement of the background structure in two specific CO_2 bands at 4.3 μm as the line-of-sight scanned the solar specular point. The second observation performed by the IBSS sensors was a solar specular point using the wide band CO_2 filter (2D). This measurement occurred at GMT 121:23:41 and produced surprising results. A significant amount of spatial variations were found in the preliminary data that was telemetered to the ground.

A vertical scan of the earthlimb during day and night was also performed by rotating the SPAS to cover the tangent altitude range from the hard warmth to the local horizontal. Earthscan observations with the IBSS radiometer were directed at the hard earth using the CO_2 and MWIR filters. Measurements were also made of the spatial clutter in the vicinity of the

solar specular point. At the conclusion of the mission a report entitled "IBSS Earth Backgrounds Experiment Quick Look Report", PL-TR-91-2157, edited by R.A. Van Tassel of the Geophysics Directorate, was prepared by those participating in the mission.

3.3 IBSS Data Analysis

The first set of 320 kbit/sec radiometer infrared data was received in late July 1991 from MRC (Mission Research Corporation) on a SUN tape cartridge. Due to incompatibilities between VAX and SUN formats of binary data, MRC became responsible for translating the data from VAX to SUN format. This process of translating and transporting the data was repeated several times by Visidyne and MRC over a period of three weeks before the data format was correct and the files could be read successfully. Visidyne has not yet received all of the IBSS Earth Backgrounds data, but has received highest priority data files. Also, during this time, a 1.2 gigabyte hard drive for the SUN SPARCstation was purchased with contract funds in order to support the expected large volume of IBSS data.

The next large effort was in reading and interpreting the data format and information available. The data are subject to many regions of data dropouts which have been handled in a certain manner by the IBSS Data Processing team (Phillips Lab, MRC, and Boston College). It was necessary to determine and interpret this process by which these data were treated in order to access the data appropriately. This was accomplished through several informal conversations with MRC.

Once these problems were solved the development of analysis software began. Some analysis tools had previously been written for a quick-look of the telemetry data and were used as building-blocks for the analysis software. Presently, a program has been written to allow a user to access desired IR radiometer data and apply certain analysis tools. The analysis tools which exist are the following:

1. Spike Removal
2. 1st, 2nd, or 3rd Order Detrending
3. Mean and Variance of Time Series
4. Periodogram
5. Auto/Cross Correlation Functions

6. Probability Distribution Function

7. Exceedance Histograms

8. 1st Difference

These routines have been tested and verified, but some modifications remain. Regions of spikes and dropouts will be analyzed for their effects on statistical analyses, and a proper method for treatment will be determined and modifications to the software followed accordingly. Other plans are to implement a more accurate estimation of the Power Spectral Density. A Blackman and Tuckey method is under consideration at this time.

Using this program we have been able to begin analysis of various Earth Backgrounds Experiments (CO_2 Earthscan, Solar Specular Point - 2D, and Earthlimb Limb to Earth). Preliminary results have been reported by the Principal Investigator, R.A. VanTassel. In addition to the radiometer data we have received visible LLLTV data which has been anticorrelated with the IR data for some of the Earthscan data.

Future plans include receipt of the full set of Earth Backgrounds data and also the SPAS and Orbiter Attitude and Ephemeris data in VAX floating point format. This will require a program to be written to convert the data to SUN floating point format. From this data various pointing information will be calculated (tangent height, LOS Earth-track, solar angles - lighting conditions, etc.). These parameters are necessary for a complete analysis of the radiometer data. A table will be generated with these parameters for every second during each Backgrounds experiment as well as being presented in a graphical format. An effort is in effect to prepare a compendium report on all or most of the Backgrounds data. This report will include all necessary pointing and ancillary information and analysis as described above.

3.3.1 IBSS Programming Status

Programs have been written in-house to analyze radiometer data from the IBSS experiment. There is approximately one gigabyte of radiometer data on a 1.2 gigabyte hard disk connected to Visidyne's SUN SPARCstation server. The programs, listed in Table 1, have been written in IDL (Interactive Data Language) operating within a UNIX environment.

I-Values, Q-Values, amplitude, radiance, phase, or filter wheel positions can be viewed and plotted. Data can be detrended and spikes can be removed. Correlation, exceedance, first differencing, periodogram, and PDF analysis are presently available within the program.

Table 1

PROGRAM	PROGRAM DESCRIPTION	COMMON BLOCKS	CALLED BY	ROUTINES CALLED
ARRAYFIX	Puts 2-d detector data into 1-d array and calculates time.	COMARRAYS COMVALUES	GET_DETECTOR	
ASSIGNPLOT	Assigns plot numbers to plot about to be worked on.	COMPLOT	CROSSCORR EXCEDANCE FIRSTDIFF PDF PLOTDATA PSDDATA REMSPIKE	
CALIBRATE	Applies calibration to data and produces radiance array	COMARRAYS COMVALUES COMPLOT	GET_DETECTOR	
CROSSCORR	Calculates both auto and cross correlations.	COMARRAYS COMVALUES COMPLOT	PLOTDATA	ASSIGNPLOT
DETREND	Detrends data in plot last selected.	COMARRAYS COMVALUES COMPLOT	PLOTDATA	ASSIGNPLOT
EXCEEDANCE	Calculates the exceedance.	COMARRAYS COMVALUES COMPLOT	PLOTDATA	ASSIGNPLOT

IBSS IDL ROUTINES

8

Table 1 (Cont.)

IBSS IDL ROUTINES				
PROGRAM	PROGRAM DESCRIPTION	COMMON BLOCKS	CALLED BY	ROUTINES CALLED
FILELOOK	Does entire operation on a specified file.	COMARRAYS COMVALUES COMPLOT	IBSSLOOK	OPENFILE GET_DETECTOR PLOTDATA
FIRSTDIFF	Calculates the first difference.	COMARRAYS COMVALUES COMPLOT	PLOTDATA	ASSIGNPLOT
FWPFIX	Makes 1-d array of filter wheel position.	COMARRAYS COMVALUES	OPENFILE	—
GET_DETECTOR	Pulls out detector info from file.	COMARRAYS COMVALUES	FILELOOK	ARRAYFIX CALIBRATE
IBSSLOOK	Highest level of program.	COMARRAYS COMVALUES	—	FILELOOK
OPENFILE	Retrieves header info.	COMARRAYS COMVALUES	FILELOOK	FWPFIX
PADDATA	Applies a padding equal to the size of the array for FFT.	—	PSDDATA	—
PDF	Calculates the Power Density Function.	COMARRAYS COMVALUES COMPLOT	PLOTDATA	ASSIGNPLOT

Table 1 (Concl.)

IBSS IDL ROUTINES				
PROGRAM	PROGRAM DESCRIPTION	COMMON BLOCKS	CALLED BY	ROUTINES CALLED
PLOTDATA	Plots, replots and calls analysis tools.	COMARRAYS COMVALUES COMPLOT	FILELOOK	ASSIGNPLOT CROSSCORR EXCEDANCE FIRSTDIFF PSDDATA PDF SPIKEOUT
PSDDATA	Calculates the PSD.	COMARRAYS COMVALUES COMPLOT	PLOTDATA	ASSIGNPLOT PADDATA
SPIKEOUT	Removes spikes from data.	COMARRAYS COMVALUES COMPLOT	PLOTDATA	ASSIGNPLOT

IBSSLOOK is the main program which calls other programs used for this analysis. The program is primarily menu driven and responds to the mouse. This program was devised so that any detector data (from 32 detectors), from any file, could be made of any plot. Information pertaining to ten plots can be stored, and one to four plots can be plotted per page. The plots for the multiplots can be any of the ten stored plots in any order. One to four detectors can be opened at any one time. These capabilities result in many plot page variations being available.

3.3.2 Tabular and Graphical Presentations of IBSS Data

During this period a program was developed to determine the latitude, longitude, and altitude of the tangent point as observed by the SPAS during an earthlimb experiment. For an earthsweep experiment the latitude and longitude of the intersection point on the SPAS line-of-sight is determined. This information can then be presented in the form of a graph showing latitudes and longitudes superimposed on a map of the world. Both the SPAS position and the position of the tangent point or earth intersection point is displayed with tick marks showing two minute intervals (GMT) along the path. An example of such a graph is shown in Fig. 2. This shows the position of the SPAS on May 2 from 16:40 to 17:35 GMT corresponding to orbits 69 and 70. The two jumps in the tangent point latitude and longitude at longitudes 235° and 160° were caused when the pitch of the SPAS was being adjusted. Figure 3 shows the tangent height (km) as a function of elapsed time for the same two orbits. The two peaks occur when the pitch was being changed.

4.0 CIRRIS IA OPERATIONS SUPPORT

Visidyne contributed a variety of supporting tasks in connection with the CIRRIS IA Experiment (Cryogenic Infrared Radiance Instrumentation for Shuttle) flown on the Shuttle Flight STS-39 which was launched on April 28, 1991 and ended on May 6, 1991.

4.1 Flight Operations Support

Visidyne's participation on the CIRRIS 1A flight operations team required attendance at all of the Joint Integrated Simulations (JIS) at Johnson Space Center (JSC), as well as several
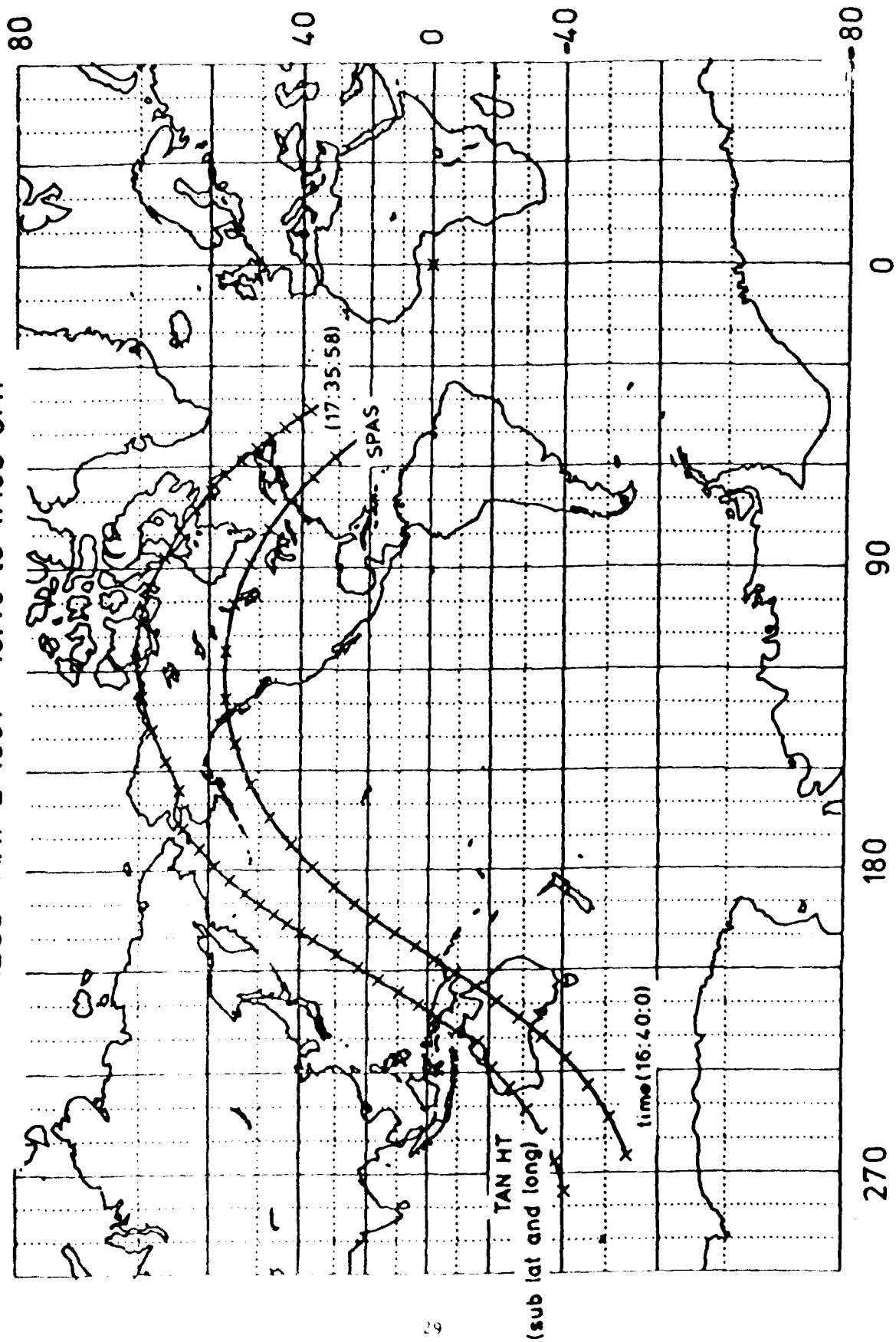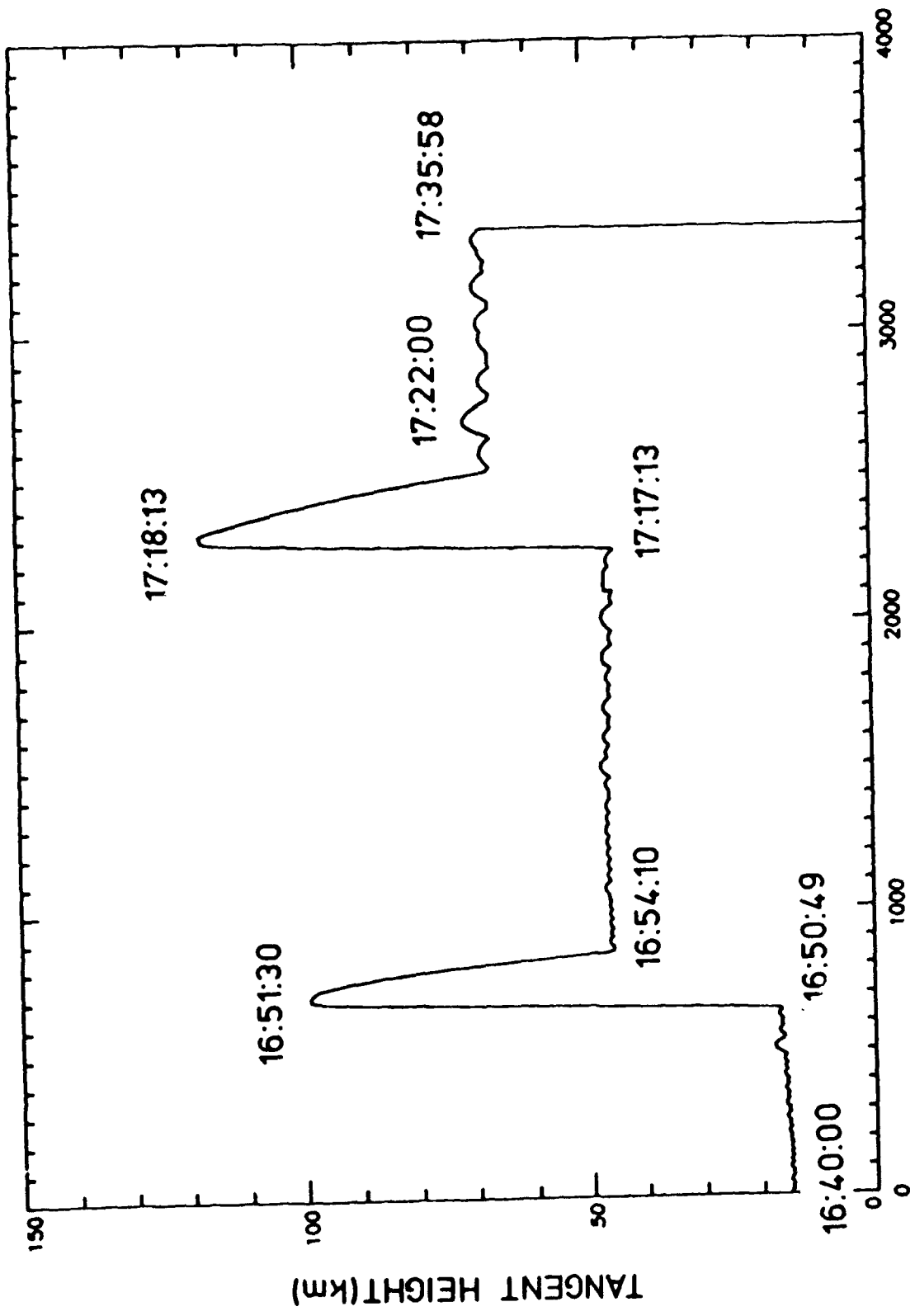
Figure 2. Position of SPAS and NADIR at the Tangent Height

Figure 3. Tangent height vs. elapsed times IBSS May 2, 1991

13

of the factory training sessions at Lockheed in Sunnyvale, CA. An additional task was technical supervision of the Trending Software development underway at Utah State University (USU).

The job of the trending and analysis engineer was to man a 12 hour/day shift during the eight day mission. The position was one of twelve on the CIRRIS 1A team at the Payload Operations Control Center (POCC) at the Mission Control Center (MCC) at JSC. At various times throughout the mission, the crew would read down, or in some way downlink, information regarding the health of the CIRRIS 1A instrument. It was the job of the Trending and Analysis Engineer to collect, format, and analyze these data in order to ascertain a long-term projection of instrument performance, and notify the CIRRIS 1A Principal Investigator (PI) of any potential problems. For example, if temperatures were seen to be rising on the laser box, a projection of at what point they would go out of limits would be made, followed by suggesting a course of action to cool them off. This happened several times throughout the mission, and thermal problems were thereby avoided.

The Trending Software was to assist the Trending and Analysis Engineer in collecting and displaying the sensor health data during the mission. Additionally, the software was to provide a limited data transfer protocol so that data could be shared over the network developed at the POCC. The data acquisition software was developed using the C language under the Santa Cruz Operations (SCO) Unix operating system and run on an 80386-based workstation at the POCC. The other machines on the network were DOS-based computers. The display software was also written in C and could be run on both the Unix and DOS systems. Preparation and training for the mission were primarily accomplished during this year at the Rockwell and NASA facilities. Involvement required numerous trips to Houston as well as several trips to Logan, UT to monitor system development. There were also flight operations meetings at various other locations, including Kennedy Space Center, FL.

4.2 Ground Operations Support

The CIRRIS 1A instrument was at Kennedy Space Center during this period of time before the Shuttle launch. Due to launch delays, the instrument was there for longer than initially anticipated. As a result, extra maintenance was required to keep the instrument in a ready-to-fly state, and support was provided in order to mitigate the additional workload required

of the existing Ground Operations team. This support included monitoring the cryogenic vacuum pumping of the instrument during the night shift due to a NASA requirement that the procedure be monitored 24 hours a day. This same requirement necessitated involvement with the final cryogenic cooling of the instrument immediately before launch.

4.3 OPUS Development

The Optical Physics User-oriented Software (OPUS) is the primary method whereby scientist can access the CIRRIS 1A data. OPUS was developed by Boston College at their Alfred Circle facility in Bedford, MA. Visidyne personnel provided the technical supervision of this effort.

OPUS is a multifaceted system which stores, sorts, processes, and displays the four gigabytes of data acquired during the CIRRIS 1A mission. OPUS is entirely menu-driven and allows the scientist on-line access to 100% of the data at all times. It has been universally acclaimed by the scientists working on the CIRRIS data as a huge improvement over the previous methods of data storage and retrieval.

OPUS development began several years ago when the CIRRIS 1A PI, and others involved in the project, realized that the CIRRIS 1A data set would be far too large to analyze the conventional batch processing. As a result, we conceived a system whereby scientists could display data at a workstation using whatever parameters they choose, alter the plots at their convenience, and produce only hard copies of the final displays. This would replace the time consuming iterative process of submitting batch jobs to the central computer facility at the laboratory and waiting for the results, only to have to re-submit the jobs with slight alterations. The OPUS software utilizes these time-tested algorithms, but packages them in a graphical user environment that is easy to use and flexible enough to handle many data analysis methods.

The development of the OPUS took several years of continual effort by the software development team, and Visdiyne monitored and contributed to this development during that time and advised the CIRRIS 1A PI on the optimum direction the development should take.

While originally developed in FORTRAN under the DEC VMS system, the OPUS now runs under the Unix operating system. This transition from VMS to Unix was a difficult decision to make and was predicated by two things. One, most of the best state-of-the-art

hardware is being developed to specifically run Unix and Unix-like operating systems. Two, the Air Force is urging its component laboratories to move toward Unix as a universal operating system for workstation environments. A good deal of the OPUS in C was rewritten in order to make the transition. All of the Input/Output (I/O) routines, for instance, would not compile under Unix FORTRAN. This included both screen I/O and file I/O. All of the windowing and graphing routines had to be rewritten in C. Initially, Boston College didn't have the manpower to accomplish this, so much of the transfer was accomplished by USU.

A database handling system was developed in order to catalog, store, and retrieve the huge CIRRIS 1A data set. This routine worked hand-in-hand with the analysis and display software to provide a continuous and completely interactive interface between the scientist and the data.

OPUS has enjoyed wide acceptance at the Phillips Laboratory, and it continues to be updated and improved. A current task is to provide a technical interface between the scientific community and the software developers in order to better achieve a quick resolution to user requirements.

4.4 Data Analysis

The advent of such large projects as CIRRIS 1A, Spirit II, and MSX have necessitated the development of the atmospheric backgrounds Data Analysis Center at the Phillips Laboratory. Visidyne has contributed to planning, developing, and operating this center. To do this required researching the computer industry in order to determine the optimum configuration of workstations and peripheral devices. This equipment included DECstation 5000s, VAXstations, Sun Sparcstations, Silicon Graphics Personal Irises, optical disk jukeboxes, and various I/O devices. So far the center has enjoyed great success in providing a reliable environment for data analysis.

5.0 MSX EARTHLIMB BACKGROUND EXPERIMENTS

MSX is a satellite-based experiment to be flown in a low-earth orbit in 1993. MSX has three primary mission objectives. The first is to collect data on representative target

16

engagements to support ground validations of midcourse surveillance and defense functions through simulations and hardware in the loop tests. The second is to collect target signature and background measurement data to improve and validate models and serve as a system design database. The third is to validate performance of key Global Protection Against Limited Strikes (GPALS) Elements Sensors (GES) technologies such as optics, infrared (IR) and visible focal plane arrays (FPAs), on-board signal processors, and contamination monitoring and mitigation.

To support GES concepts, the primary MSX sensors are a longwave infrared (LWIR) sensor, SPIRIT III (which includes both an IR radiometer and an IR interferometer), and a Space-Based Visible (SBV) sensor. These sensors are responsive to both space and ground-based sensor system concepts and requirements derived through integrated sensor architectures as defined in the System Design Document (SDD). The MSX sensor complement also includes the Ultraviolet/Visible Imagers and Spectrographic Imagers (UVISI), which will provide additional measurements data to support advanced modeling and additional validations of GES concepts. The MSX sensors are body-fixed and co-boresighted.

Visidyne is supporting the Earthlimb Background principal investigator with the design and implementation of background experiments. The effort was the design of earthlimb radiance structure measurement experiments for the MSX flights. The atmospheric limb radiance structure survey provides the database of the two dimensional measure of the spatial structure in the limb radiance of the atmosphere. The measurements in this experiment will be performed in such a way as to provide the atmospheric limb radiance for, primarily, the radiometer wavelength bands. During the experiment, measurements performed with the interferometer and the UVISI and SBV will provide spectral measurements over the radiometer wavelength bands as well as measurements over other spectral regions. These measurements can assist in radiating species determination. The work performed consisted of determining the requirements that must be placed on the experimental management in order to obtain the desired measurement, as well as generating preliminary experimental plans. This experimental plan was submitted to the Principal Investigator and distributed to the MSX community for review. This plan is contained in a Visidyne document, VI-1656, "Earthlimb Mean and Structured Radiance (Constant Tangent Height Scan)", dated 17 June 1991.

Following this effort, work continued on the planning of other measurements for the MSX earthlimb experiment plans. Plans have been developed for the measurements of mesospheric clouds. Three separate experimental plans were written, submitted, and distributed to the MSX community for review. These are:

- VI-1739, "Earthlimb Experiment Plan ELE-12, High Latitude Enhanced Backgrounds: Mesospheric Cloud Radiance and Structure", 30 July 1991.

- VI-1740, "Earthlimb Experiment Plan ELE-16, High Latitude Enhanced Backgrounds: Mesopheric Cloud Fixed Point Experiment", 30 July 1991.

- VI-1741, "Earthlimb Experiment Plan ELE-17, High Latitude Enhanced Backgrounds: Mesospheric Cloud Coordinated MSX/Ground Site Measurements", 30 July 1991.

In addition a fourth experimental plan, ELE-11, "High Latitude Enhanced Backgrounds: Stratospheric Warming", was started and will be completed later in 1991.

On the next five pages, one page summaries of the five experimental plans are included herein for reference.

In support of the MSX, a number of computer programs have been generated. Some of these are described below:

1. Terminator Program and a more Accurate Solar Ephemeris Program

Terminator Program was set up to calculate sun's evaluation angle for 0, -6, -12, and -18 degrees corresponding to terminator line, civil, nautical, and astronomical twilight. In addition, the sunrise/sunset line (sun's center being 50 min below horizon) was also calculated. These calculations were made by iteration. The time was adjusted until the proper elevation angle was achieved at the chosen location.

A more accurate solar ephemeris program was developed by using Meeus equations to full accuracy[1]. An accuracy verification was made by comparing the sun's daily right ascension (RA), declination (DEC), and radius vector values as obtained from Meeus equations against values obtained from The 1992

EXPERIMENT TITLE: ELE-2 -- Limb Radiance and Structure : Constant Tangent Height Survey

INTERNAL PRIORITIZATION: 1 of 19

OTHER PI INVOLVEMENT: Coordination with STB

EXPERIMENT OBJECTIVE:
ELE-2 will provide a data base of earth limb mean and structured radiance measurements for tangent altitudes from 40-160 km. The measurements are to be made with the Spirit III radiometer primarily and the interferometer, UVISI, and SBV secondarily. The analysis of these scans will be used to determine the earth limb radiance power spectral density with sufficient precision so that mitigation algorithms can be designed, as well as provide the basis for atmospheric radiance structure models.

REQUIREMENTS SUPPORTED:
SRD Requirements   2.3.1 Atmospheric Limb Radiance Profile and Spectra (EL-1)
                        2.3.2 Atmospheric Limb Radiance Clutter (EL-2)
SMRD Requirements   4.1, and 4.7

MSX INSTRUMENTATION:
Mandatory: SPIRIT III radiometer
Required: SPIRIT III interferometer
             UVISI Imagers (used sequentially) and spectrometers; SBV full frame mode
Desired: Contamination, all passive sensors

COROLLARY/AUXILLIARY INSTRUMENTATION:
Auxiliary Data:
    -DMSP: Operational Line Scan, J4 sensor
    -GOES: magnetometer and particle data
    -TIROS-N Operational Vertical Sounder (TOVS): upper altitude height fields
    -Meteorological Satellite: imagery data
    -UARS: temperature and minor constituent profiles and limb emissions
    -Optical and radar measurements from the CEDAR network

OPERATIONAL SCENARIO:
The Spacecraft will be moved from park to view the limb at tangent height altitude of 40 km with a azimuthal angle relative to vehicle heading of plus or minus 90°. The radiance will be measured using a Coolie Hat Drift scan on this line-of-sight over a latitude span of 90° requiring 26 minutes. This measurement sequence is repeated at tangent attitudes of 60, 80, 100, 140, and 160 km over all latitudes and seasons. Data is recorded at the 5 Mbps rate. These measurements will be repeated a sufficient number of times to generate a global, seasonal, and altitude limb mean and structured radiance database.

SPECIAL CONSIDERATIONS:
None

EXPERIMENT TITLE: ELE-12 -- High Latitude Enhanced Backgrounds: Mesospheric Cloud Radiance and Structure

INTERNAL PRIORITIZATION: 15 of 19

OTHER PI INVOLVEMENT: STB

EXPERIMENT OBJECTIVE:
Mesospheric clouds (MC) may interfere with observations of targets above the hard earth. They occur in thin (1-2 km thick) structured layers located near the mesopause altitude of 83 km during mid- to high-latitude summer conditions. The existence, location, spatial distribution and persistence of MC will be measured in the horizontal and vertical dimentions. ELE-12 will be performed as a function of geographic parameters, season, time of day, geomagnetic index, etc. To achieve the total global, seasonal, and earth limb mean and structured radiance database that is required, ELE-12 will be repeated a large number of times.

REQUIREMENTS SUPPORTED:
SRD Requirement   2.3.7 Noctilucent Clouds (NCL) and Polar Mesospheric
                        Clouds (PMC) (EL-7)
SMRD Requirement   4.6 Polar Mesospheric and Noctilucent Clouds,
                        4.7. Polar Mesopheric and Noctilucent Cloud Deficiencies

MSX INSTRUMENTATION:
Mandatory: SPIRIT III radiometer, and interferometer
            UVISI: IUW, IVW, IUN IVN and SPIM1 to SPIM5
            SBV, full frame mode (not processed)
Desired: TQCM, CQCM, MASS Spectrometer, Pressure gauge

COROLLARY/ANCILLARY INSTRUMENTATION:
Auxiliary Data:
    -DMSP: Operational Line Scan, Low Light Level Imager, J4 sensor
    -GOES: magnetometer and particle data
    -TIROS-N Operational Vertical Sounder (TOVS): upper altitude height fields
    -Meteorological Satellite: imagery data
    -UARS: temperature and minor constituent profiles and limb emissions
    -Optical and radar measurements from the CEDAR network
    -USAF rocketsonde probe sounding

OPERATIONAL SCENARIO:
In the northern hemisphere the spacecraft is moved from park when crossing 82°N on ascent, to view the limb with the lowest radiometer pixel at the tangent altitude of 60 km. The radiance is measured using the Coolie Hat Drift scan along a line-of-sight at --165° with the velocity vector. Data is recorded at the 5 Mbps rate. These measurements will be repeated a sufficient number of times to generate a statistical data base.

SPECIAL CONSIDERATIONS:
None.

EXPERIMENT TITLE: ELE-16 -- High Latitude Enhanced Backgrounds:
Mesospheric Cloud Fixed Point Experiment

INTERNAL PRIORITIZATION: 16 of 19

OTHER PI INVOLVEMENT: STB

EXPERIMENT OBJECTIVE:
Mesospheric clouds (MC) may interfere with observations of targets at low tangent
altitudes. They occur in thin (1-2 km thick) structured layers located near the
mesopause altitude of 83 km at mid- to high-latitude summer conditions The lack of a
definitive data base and model of the radiant intensity, spatial structure and cloud
morphology of MC is a critical deficiency. An uncertainty in the model exists as to the
particle size distribution. The goal of experiment ELE-16 is to measure the emission
from a given fixed mesospheric cloud over a wide range of scattering angles which is a
very sensitive function of the particle size of the scattering medium. The experiment
ELE-16 will be performed only after the measurements of ELE-12 have determined
that the MSX instruments are able can measure MC emissions.

REQUIREMENTS SUPPORTED:
SRD Requirements   2.3.7 Notctilucent Clouds and Polar Mesospheric Clouds
SMRD Requirements   4.1, 4.4, 4.7

MSX INSTRUMENTATION:
Mandatory: SPIRIT III radiometer and interferometer,
              UVISI: IUN and SPIM1 to SPIM5, SBV, full frame mode (not
              processed)
Desired: Contamination Passive Sensors

COROLLARY/ANCILLARY INSTRUMENTATION:
Auxiliary Data:
    -DMSP: Operational Line Scan, Low Light Level Imager, J4 sensor
    -GOES: magnetometer and particle data
    -TIROS-N Operational Vertical Sounder (TOVS): upper altitude height fields
    -Meteorological Satellite: imagery data
    -UARS: temperature and minor constituent profiles and limb emissions
    -Lidar measured constituent profiles
    -Optical and radar measurements from the CEDAR network

OPERATIONAL SCENARIO:
In the northern hemisphere, experiment ELE-16 starts when the spacecraft crosses the
latitude 35° on ascent, with the spacecraft moved to achieve a tangent altitude of 60 km
for the lowest radiometer pixel. The radiance is measured along a changing line-of-
sight which tracks a given fixed point at 83 km tangent altitude. The measurement
time is ~15 minutes. Depending on the latitude of the tracked point, a second point
may be selected for tracking during a given orbit.

SPECIAL CONSIDERATIONS:
Fixed point track algorithms. Sun illumination at altitudes of 75 km and high

EXPERIMENT TITLE: ELE-17 High Latitude Enhanced Backgrounds: Mesospheric Cloud Coordinated MSX/Ground Site Measurements

INTERNAL PRIORITIZATION: 17 of 19

OTHER PI INVOLVEMENT: STB

EXPERIMENT OBJECTIVE:
Experiment ELE-17 will be performed, using ground assets and rocket-borne instruments, to determine the various parameters necessary for a proper model of polar mesospheric and noctilucent clouds. The experiment ELE-17 will be performed only after the measurements of ELE-12 have determined that the MSX instruments can measure MC emissions. In ELE-17 it is anticipated that the ground assets of incoherent radar, photometers and all-sky imagers at Poker Flat, Alaska will be used. If successful, this experiment would perform the first simultaneous measurement of a noctilucent and polar mesospheric cloud. Visual sightings of the NLC would be made from a location south of Poker Flats at a time when the ground observer is in the dark and the cloud is in the sunlight. This experiment could also be performed over ranges with similar ground assets such as Kiruna, Sweden.

REQUIREMENTS SUPPORTED:
SRD Requirement   2.3.7 Noctilucent Clouds (NCL) and Polar Mesospheric
                         Clouds (PMC) (EL-7)
SMRD Requirement   4.1, 4.4, 4.7

MSX INSTRUMENTATION:
Mandatory: SPIRIT III radiometer and interferometer
Required: UVISI: IUN and SPIM1 to SPIM5, SBV, full frame mode (not
              processed)
Desired: TQCM, CQCM, MASS Spectrometer, Pressure gauge

COROLLARY/ANCILLARY INSTRUMENTATION:
Auxiliary Data:
    -DMSP: Operational Line Scan, Low Light Level Imager, J4 sensor
    -GOES: magnetometer and particle data
    -TIROS-N Operational Vertical Sounder (TOVS): upper altitude height fields
    -UARS: temperature and minor constituent profiles and limb emissions
    -Optical and radar measurements from the CEDAR network
    -USAF rocketsonde probe sounding

OPERATIONAL SCENARIO:
The timeline for experiment set ELE-17 starts when the satellite is approaching the geographic pole in the northern hemisphere. The spacecraft is moved from park to viewing a position at tangent altitude of 60 km for the lowest radiometer pixel. The radiance is measured along a line-of-sight which tracks the point above Poker Flats at 83 km tangent altitude. Measurement time is approximately 10 minutes above the ground site. .

SPECIAL CONSIDERATIONS:
Constant point tracking algorithm. The experiment sun illumination at 83 km and a solar depression of 6 to 12 degrees from the ground site.

EXPERIMENT TITLE: ELE-11 -- High Latitude Enhanced Backgrounds: Stratospheric Warming

INTERNAL PRIORITIZATION: 19 of 19

OTHER PI INVOLVEMENT: STB

EXPERIMENT OBJECTIVE:
Current earthlimb radiance models do not cover known strong radiance excursions such as stratospheric warming events. These extreme conditions may create infrequent but important system outage conditions. These events take place in the arctic regions once or twice a year, and cause long-lived massive changes in atmospheric temperature structure. The measurement data requirement consists of atmospheric limb radiance, structure, and spectral data specific to the geographic region of the stratwarm. Operation of this experiment in an interactive mode such that ground commands could initiate the experiment after detection of a stratwarm by normal meteorological methods is desired.

REQUIREMENTS SUPPORTED:

SRD Requirement   2.3.5 Atmos. Limb Radiance - Stratwarming Event Spatial and Spectral Structure
SMRD Requirement   4.1, 4.4, 4.7

MSX INSTRUMENTATION:
Mandatory: SPIRIT III radiometer, and interferometer
             UVISI: IUW, IVW, IUN IVN and SPIM1 to SPIM5
             SBV, full frame mode (not processed)
Desired: TQCM, CQCM, MASS Spectrometer, pressure gauge

COROLLARY/ANCILLARY INSTRUMENTATION:
Auxiliary Data:
   -DMSP: Operational Line Scan, Low Light Level Imager, J4 sensor
   -GOES: magnetometer and particle data
   -TIROS-N Operational Vertical Sounder (TOVS): upper altitude height fields
   -Meteorological Satellite: imagery data
   -UARS: temperature and minor constituent profiles and limb emissions
   -Optical and radar measurements from the CEDAR network
   -USAF rocketsonde probe sounding

OPERATIONAL SCENARIO:
Earthlimb radiance and spectral intensity measurements will be made during conditions of stratospheric warming. The instrument LOS scans will encompass the stratwarm region and map the temperature and radiance distribution in the 30-150 km LOSTA range. The UV/Visible instrument will be operated in coordination with this experiment in order to determine the effects of stratwarms on radiance and structure in these bands. The data handling rate is 5 mbps for the CH draft and 25 mbps for the CHMS modes.

SPECIAL CONSIDERATIONS:
Experiment cueing by MSX or meteorological satellite observations.

Astronomical Almanac. The results are shown in Fig. 4. The maximum error due to RA and Dec is less than six arc seconds. The maximum error in radius vector is 2250 kilometers, which is an error of about 1.3×10^{-5} AU.

2. **Performed Twilight Calculations for Poker Flat, Alaska and western Siberia**

   This was done by using the Terminator Program described above. The calculations performed were needed to ascertain orbits which should be chosen to meet the criterion for Mesospheric Cloud (MC) measurements.

3. **Improved Satellite Orbital Program**

   A previous satellite program was modified to include the calculation of a satellite's geodetic latitude and height by iteration, as suggested in the Astronomical Almanac.

4. **Calculated Orbital Elements for MSX Satellite**

   Elements which defined the MSX orbit were specified by the Applied Physics Lab (APL) of the Johns Hopkins University. The difference in the elements between the program in 3. above and that of APL was well within orbit injection accuracy.

5. **Using the Programs of 4 Above, performed feasibility studies on:**

   a.   MC observations simultaneously for ground and satellite around Poker Flat. If simultaneously a sounding rocket is to be launched, the time window is only one to two weeks.

   b.   Using observation sites in western and eastern Siberia for MC studies.

   c.   Calculating paths scanned by varying the azimuth angle of the instrument. Determined that a great variety of locations are possible for MC studies.

6. **Developed an Improved Graphics Program to Display the Above Data on a World Map**

   A previously developed graphics program was modified to allow the projection of the orbital track and world coordinates from different center projection points. By choosing point, the graph will display the orbital track to the best advantage. Figure 5 shows MSX track as viewed from a point south of Alaska and Fig. 6 shows the same track as viewed from a point east of Greenland.
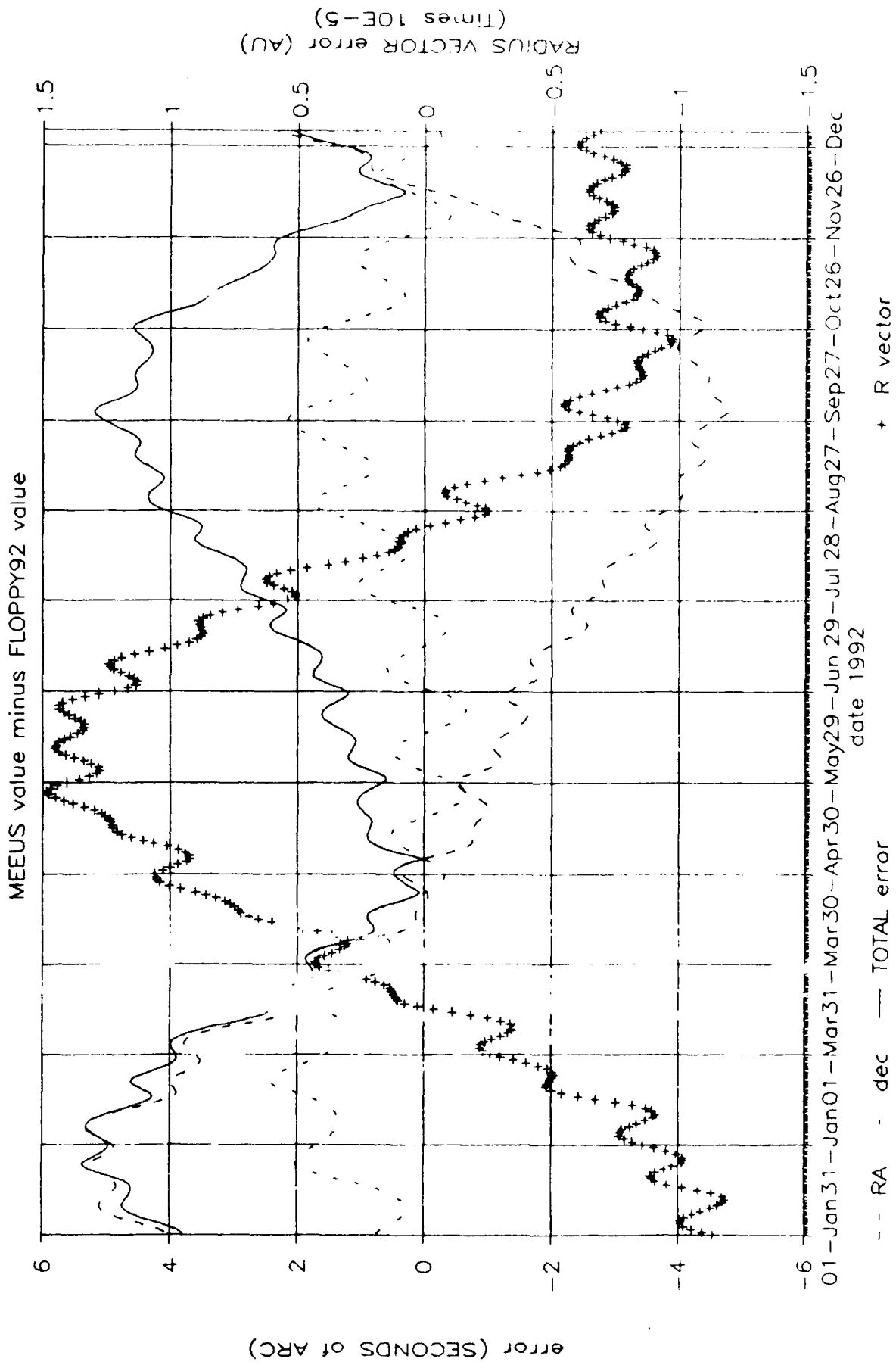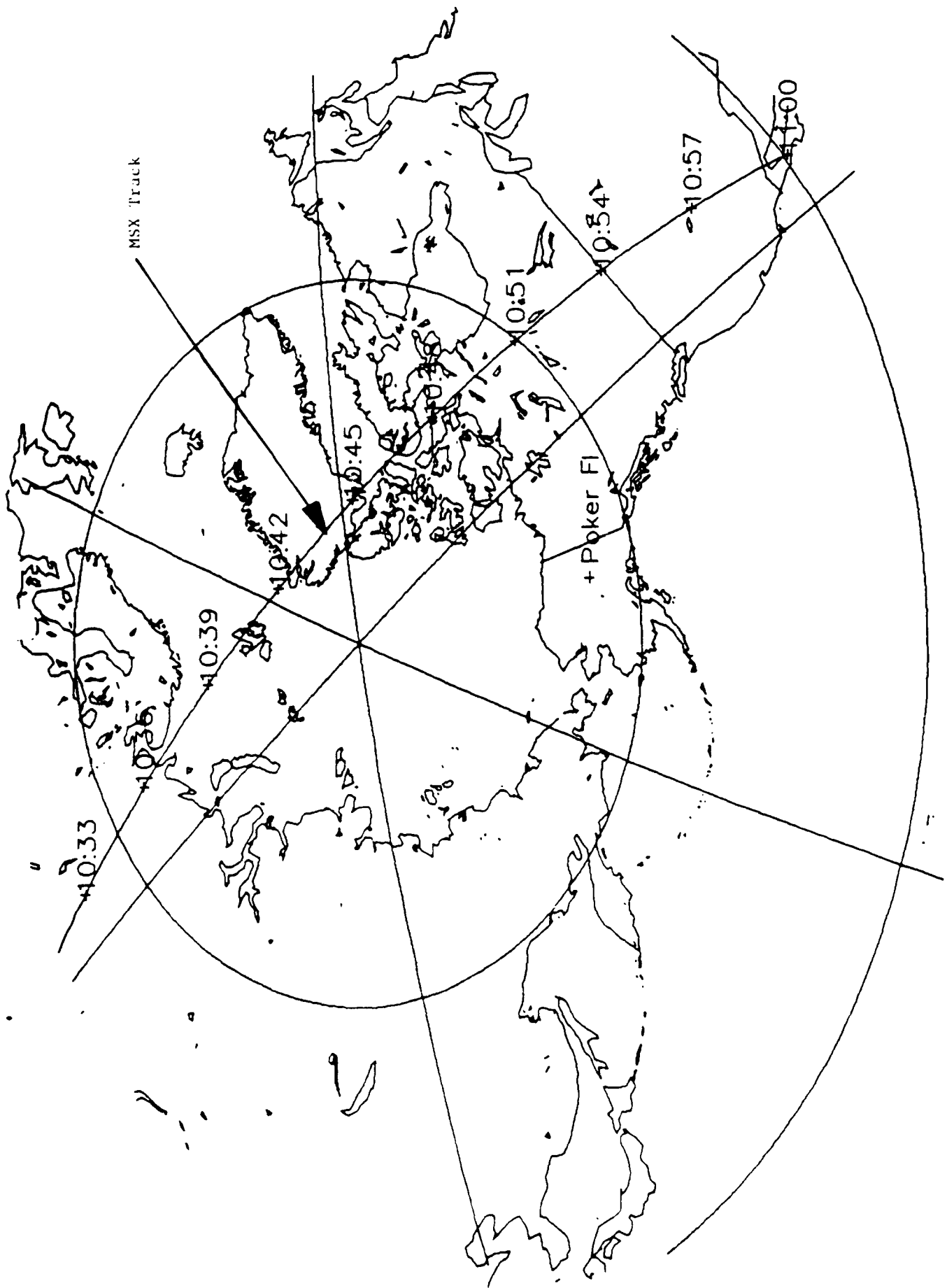
Figure 4. Solar coord comparison - exact method
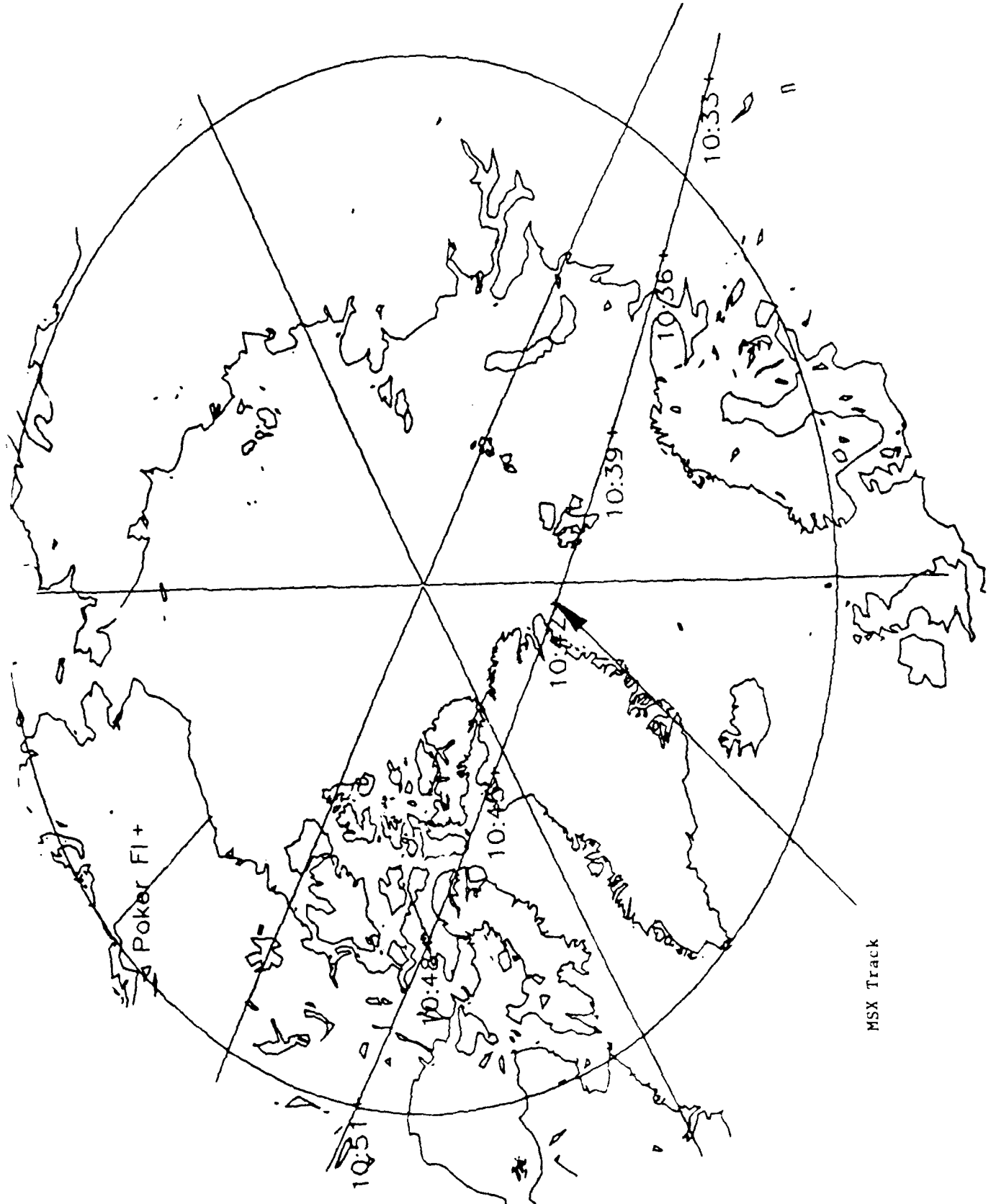
Figure 5. MSX Track as Viewed from a Point South of Alaska

Figure 6. MSX Track as Viewed from a Point East of Greenland

MSX Track

Poker Fl +

10:33

10:36

10:39

10:43

10:48

10:53

6.0 ATMOSPHERIC INTERACTIONS MODELING

6.1 Introduction

Water vapor outgassing in a space environment is a well documented phenomenon. Its effect on optical sensor performance in terms of both long term degradation and the optical environment through which sensors must operate has recently drawn the attention of the space community. This cloud of water vapor, through its interaction with the ambient atmosphere, may generate significant infrared emission.

For many years the vibrational excitation of H_2O by high velocity collisions with atomic oxygen has been identified as a potentially strong radiation mechanism at 2.7 μm. In addition, H_2O traveling at high velocities has sufficient kinetic energy to react chemically with atomic oxygen, overcoming the energy barrier (endothermicity) that exists at room temperature. This reaction produces excited hydroxyl radicals that radiate in the 3 μm spectral region ($\Delta v = 1$) and in the 1.5 μm region ($\Delta v = 2$). For the more energetic cases ($v \geq 6$ km sec) the overtone emissions are predicted to be as intense as the fundamental emissions. There is an increasing database of laboratory and field measurements that support these mechanisms[2-6].

6.2 Outgassing

There is a long history of ad hoc measurements of significant outgassing accompanying sounding rockets and spacecraft, including the space shuttle. NASA and the Air Force have compiled a large list of materials deemed unacceptable for spaceflight because of their long term outgassing properties. In addition, the history of high vacuum laboratory systems is replete with the long term "stubborn" nature of water vapor coming from insulation, potting compounds, wire harnesses, etc. More recently, room temperature outgassing measurements of re-entry coatings such as silica phenolics, carbon-carbon phenolics, and multilayer insulation have been made by a number of independent laboratories[7-11]. Very careful mass spectrometer measurements made by the University of Pittsburgh investigators confirm that after a very few seconds water vapor comprises $\geq$ 99% of the effluent. Phenolic heat shield materials typically have outgassing rates that, after 20 minutes in vacuum, are decreasing slowly ($t^{-1/2}$ time dependent) with asymptotic rates of about 10^{16} mol. cm^{-2} sec^{-1}. The MLI outgassing, however,

decays with a t^{-2} time dependence at long times. The accepted physical and model consists of a three step process. Initially a surface layer of adsorbed H_2O "peels" off quickly; then, water vapor molecules adsorbed on surface layers buried deeper in the material slowly "random walk" their way out to the vacuum. The very long time effluents come from H_2O trapped in the molecular lattice itself or actually bonded to the chemical compounds (so-called deep water). A source term of 10^{16} mol. cm^{-2} sec^{-1} is used for the calculations performed herein.

6.3 Low Altitude H_2O Emissions

6.3.1 Excitation Mechanisms

Energetic oxygen atoms interact with water molecules by two mechanisms; chemical reaction and collisional (T-V) energy transfer. As discussed previously, the chemical reaction

$$O + H_2O \rightarrow 2\ OH(v)$$
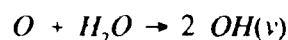
produces highly vibrationally excited OH radicals that emit at 3 μm ($\Delta v = 1$ cascade) and 1.5 μm ($\Delta v = 2$ cascade). The rate constants for the production of the OH($v=1$) and OH($v=2$) radicals are given by

$$k(OH)_{1,7} = 6.6E(-11)\ e^{-1.2eV/E_{coll}} \quad (cm^3\ sec^{-1})$$

$$k(OH)_{1,5} = 6.6E(-11)\ e^{1.6eV/E_{coll}} \quad (cm^3\ sec^{-1})$$

respectively, where E_{coll} is the center of mass collision energy (eV) between the O atom and the H_2O molecule[12]. We have taken rate constants determined from a high temperature measurement of Albers, et al. (T $\leq$ 2000 K), adjusted the activation energy to account for the additional excitation into $v = 1$ and $v = 2$, and extrapolated the expressions to energy regions of interest.

The collisional excitation mechanism

$$O + \to H_2O(v) + O$$
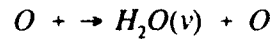
results in vibrationally excited H_2O molecules that emit primarily at 2.7 and 6.3 μm. The rate constant for the collisional excitation of water vapor in the 2.7 μm band is given by[13]

$$k(H_2O)_{2.7} = 3.4E(-11) \cdot E^{1.34}coll \cdot e^{-0.46eV/E_{coll}} \ (cm^3 \ sec^{-1})$$

The rate constants for the O atom/H_2O processes for a few velocities appropriate for orbital and suborbital spacecraft are evaluated by mechanisms in Table 2 and by wavelength in Table 3.

Table 2

Rate Constants for O Atom/H_2O Interactions (by Mechanisms)

Velocity (km/s)	E_{coll} (eV)	$k(OH)_{1.5}$ (cm^3 sec^{-1})	$k(OH)_{2.8}$ (cm^3 sec^{-1})	$k(H_2O)_{2.8}$ (cm^3 sec^{-1})
7	2.06	3.0E(-11)	3.7E(-11)	7.2E(-11)
5	1.05	1.4E(-11)	2.0E(-11)	2.3E(-11)
3	0.38	9.8E(-13)	2.8E(-12)	2.7E(-12)

Table 3

Rate Constants for O Atom/H_2O Interactions (by Wavelength)

$k_{1.5}$ (cm^3 sec^{-1})	$k_{2.8}$ (cm^3 sec^{-1})
3.0E(-11)	1.1E(-10)
1.4E(-11)	4.3E(-11)
9.8E(-13)	5.5E(-12)

Figure 7 shows the pseudo first order rate constants, k·[O], for a 7 km/s spacecraft as a function of altitude under solar median conditions (T_{cxo} = 1000 K). The resonance scattering excitation rate - the product of the Einstein B coefficient and the earthshine spectral irradiance (B·f) - is also plotted for comparison. At altitudes less than 500 km, the O-atom excitation mechanisms will dominate under solar median conditions. Figure 8 shows the 2.8 μm excitation rate constants for solar minimum (T_{cxo} = 600 K) and solar maximum (T_{cxo} = 2000 K) conditions. For high altitudes from 100 - 300 km, there is little variation in the rate constants with solar conditions. At higher altitudes, however, the solar maximum conditions provide a significant enhancement. Figure 9 shows the velocity dependence of the excitation cross sections.

6.3.2 Water Vapor Cloud Brightness

The apparent radiant intensity, I, (W/sr) of the water vapor cloud is given by

$$I = \frac{1}{4\pi} \, k[O] \, n \, \tau \, h\nu \quad (W \, sr^{-1})$$

where k is the rate constant for the particular process, [O] is the atomic oxygen concentration (altitude dependent), n is the water vapor outgassing rate (molecules sec^{-1}), τ is the thermalization time, and hν is the photon energy. We assume that the high velocity H_2O molecules are thermalized and therefore no longer have sufficient energy to react after undergoing three collisions. Hence, τ is given by

$$\tau = \frac{3\lambda}{V_R}$$

where λ is the atmospheric mean free path, and V_R is the vehicle velocity. Table 4 lists the atmospheric mean free path and O atom concentration (T_{cxo} = 1000 K) as a function of altitude.

H$_2$O Excitation Rates
Solar Median (T$_{exo}$ = 1000 K)
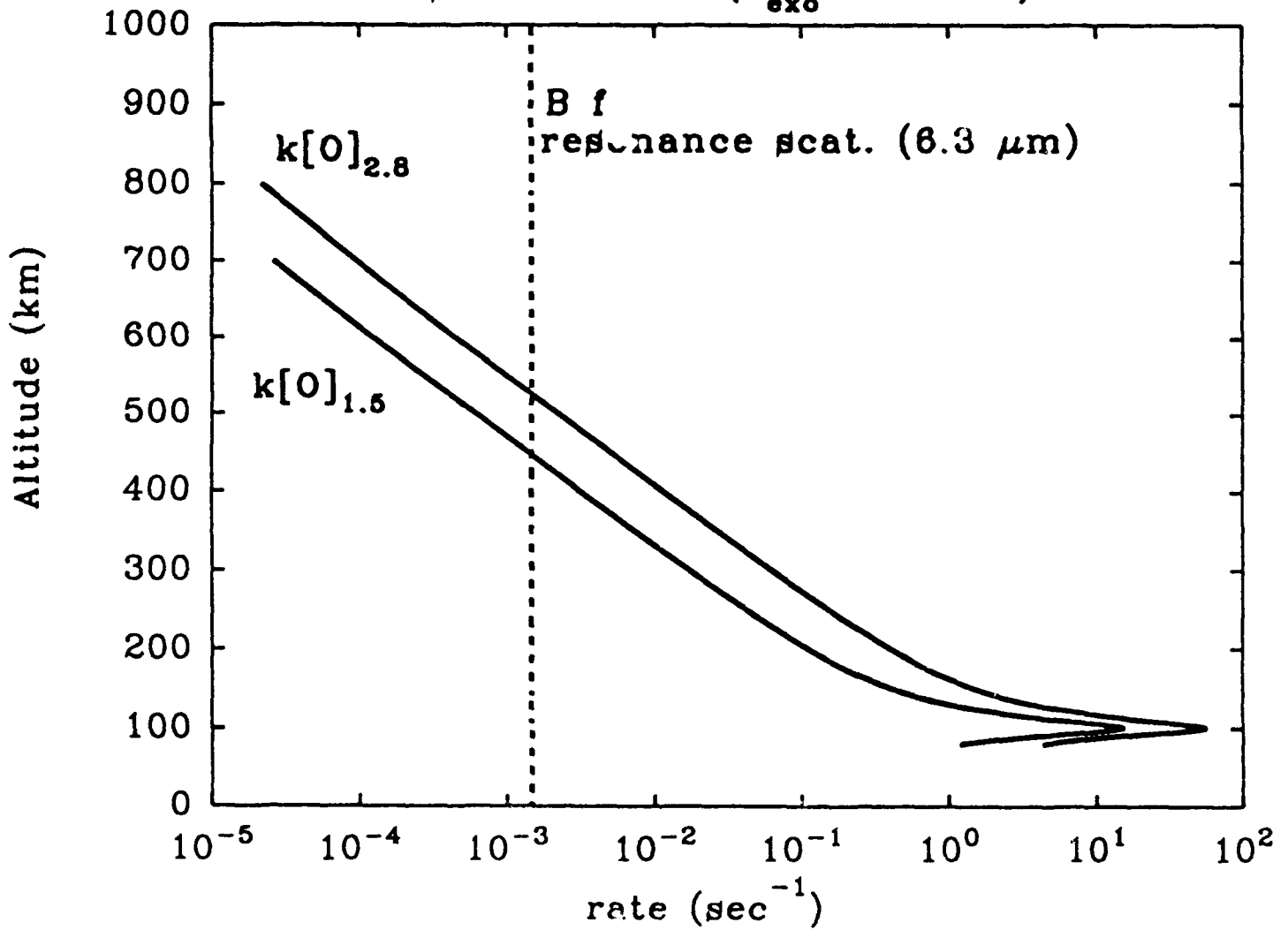
Figure 7. Pseudo first order rate constants, k·[O], for water vapor excitation at a velocity of 7 km/sec.

H₂O Excitation Rates
Exospheric Temperature Dependence
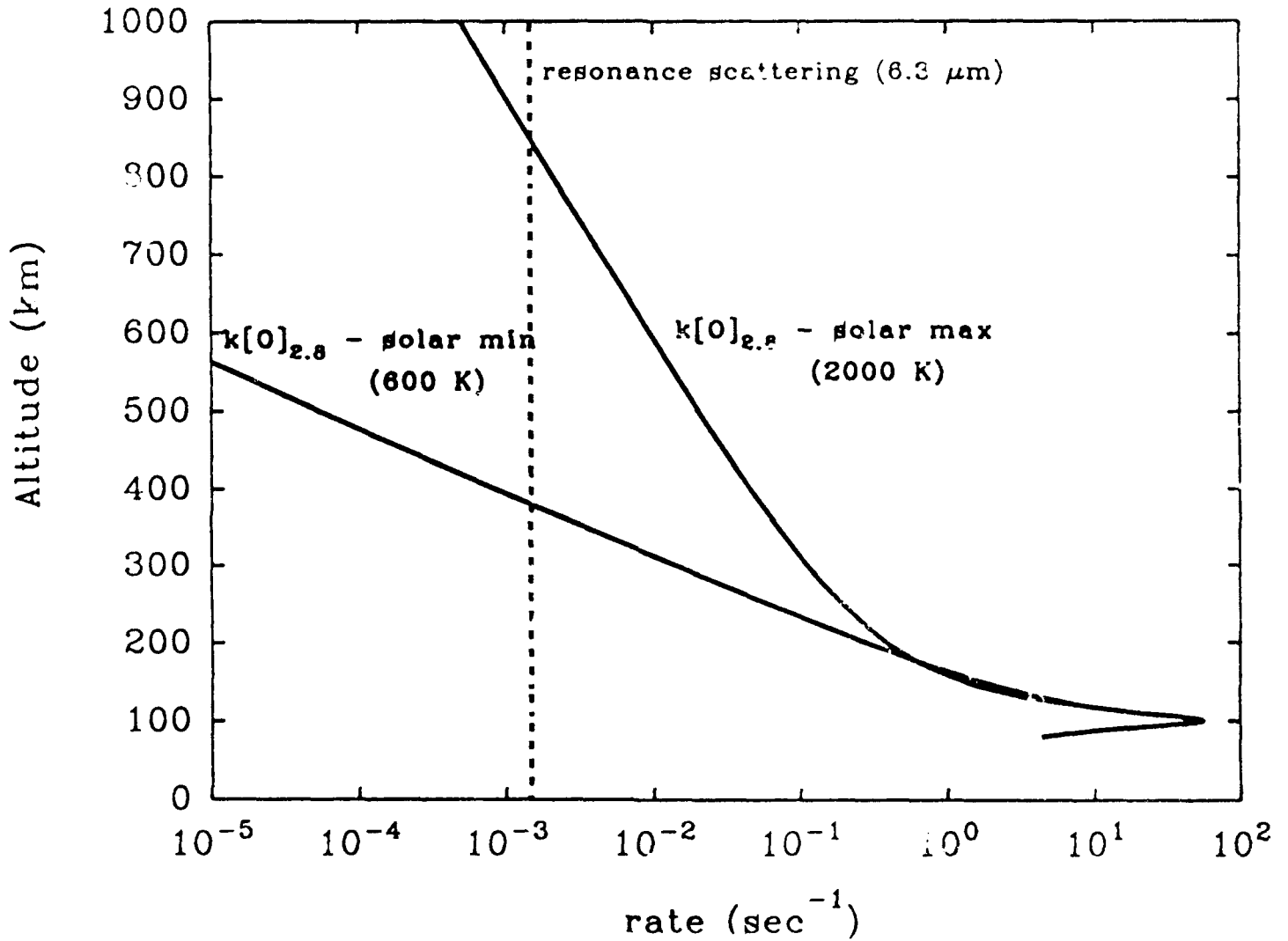
Figure 8. Rate constants for 2.8 μm excitation under solar minimum (T_{exo} = 600 K) and solar maximum (t_{exo} = 2000 K) conditions.

H_2O + O Cross sections
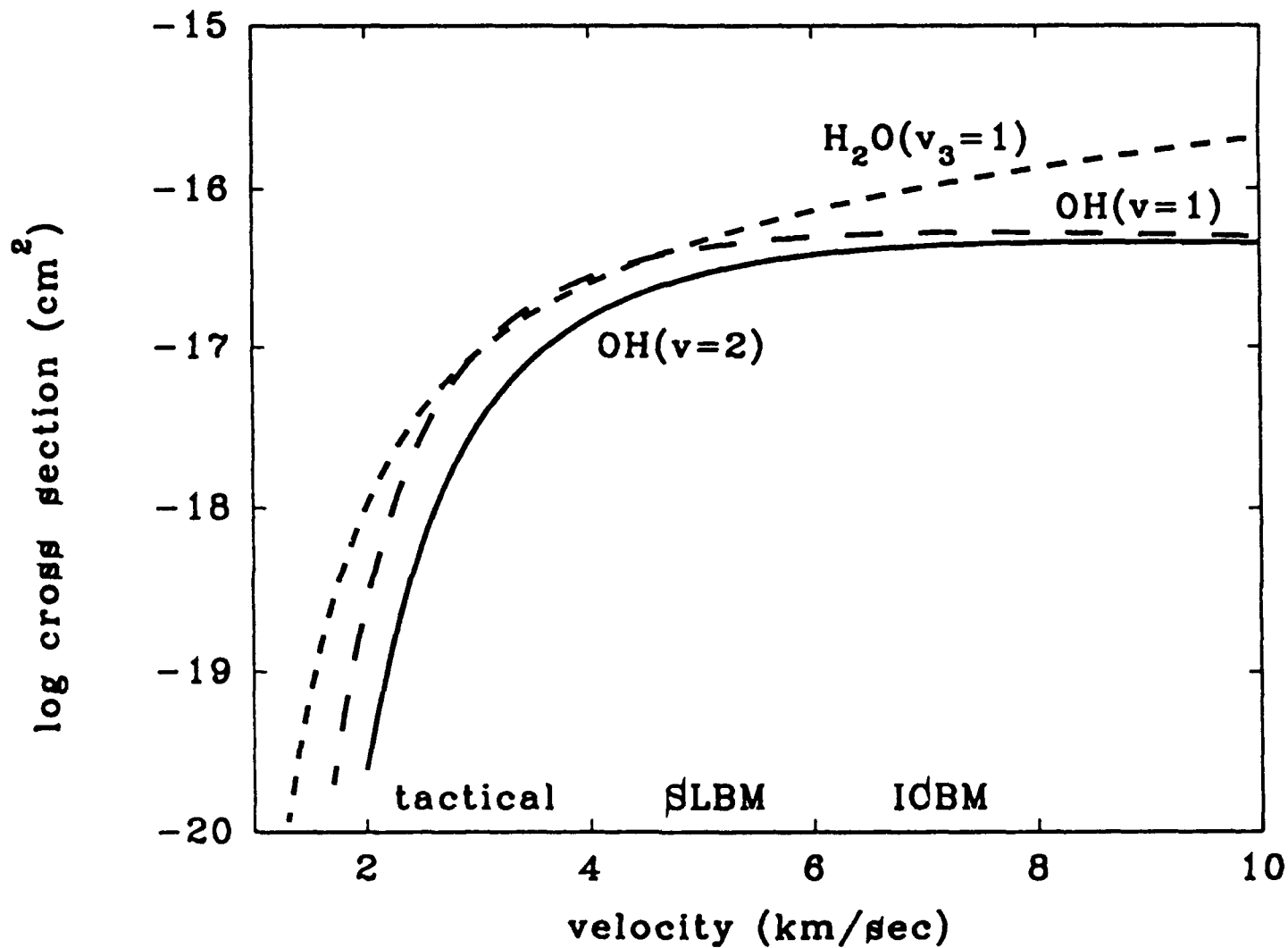
Figure 9. The velocity dependence of the excitation cross sections. The OH ($\Delta v = 1$ and $\Delta v = 2$) chemiluminescence cross-sections are obtained from a high temperature measurement of Albers, et al. The H_2O collisional excitation cross section is that used in the CHARM code.

Table 4

Atmospheric Parameters

Altitude (km)	[O] (cm^{-3})	λ (m)
125	5.0E(10)	5.6
150	1.4E(10)	33
175	6.6E(9)	100
200	3.7E(9)	240
250	1.5E(9)	890
300	5.8E(8)	2.6E(3)
500	2.0E(7)	7.7E(4)
800	2.0E(5)	1.4E(6)

This model is simple in that it does not take into account multiple collision effects or quenching. However, the model is sufficient as a first order description of the processes. A complete model of the evolution of the gas cloud could be used based on numerical solutions of the Boltzmann equations for diffusively expanding, reacting gas clouds[14]. Alternatively, a three-dimensional Monte Carlo algorithm could simulate the expansion of the gas cloud and include collisional excitation, chemistry, thermalization, radiation, and quenching.

The apparent radiant intensity of the water vapor cloud, assuming it is contained within a pixel, has an unusual altitude dependence. It is proportional to the thermalization time and to the O atom concentration.

$$I \alpha [O] \cdot \tau$$

$$\tau = \frac{3\lambda}{V_R}$$

The mean free path λ in turn is inversely proportional to the total number density.

$$\lambda \propto \frac{1}{[N_2] + [O] + [O_2]}$$

The total density, for the altitudes of interest, can be taken as the sum of molecular nitrogen, atomic oxygen, and molecular oxygen concentrations. The radiant intensity is therefore directly proportional to the O atom concentration and inversely proportional to the total concentration.

$$I \propto \frac{[O]}{[N_2] + [O] + [O_2]}$$

The radiant intensity is proportional to the fraction of the collisions occurring with oxygen atoms; therefore, the intensity of the cloud will follow the mixing fraction of atomic oxygen. This mixing fraction, and hence the radiant intensity, increases with altitude up to approximately 300 km. Figure 10 shows the O atom concentration and the O atom mixing ratio as function of altitude. The water vapor cloud apparent radiant intensity will increase with increasing altitude until either the cloud becomes larger than the pixel footprint or until atomic oxygen becomes the dominant species in the atmosphere.

At some altitude (and range), the water vapor cloud will expand outside a single sensor pixel. In this limit, the apparent single pixel radiant intensity is given by

$$I = \frac{1}{4\pi} k[O] \, n \, \tau \, h\nu \, \frac{\Omega R^2}{\pi r_{cl}^2}$$

where Ω is the pixel solid angle, R is the range to the vehicles, and r_{cl} is the radius of the outgassed cloud. The cloud size, with aspect to the object, is given by

$$r_d = \tau \, V_{th}$$

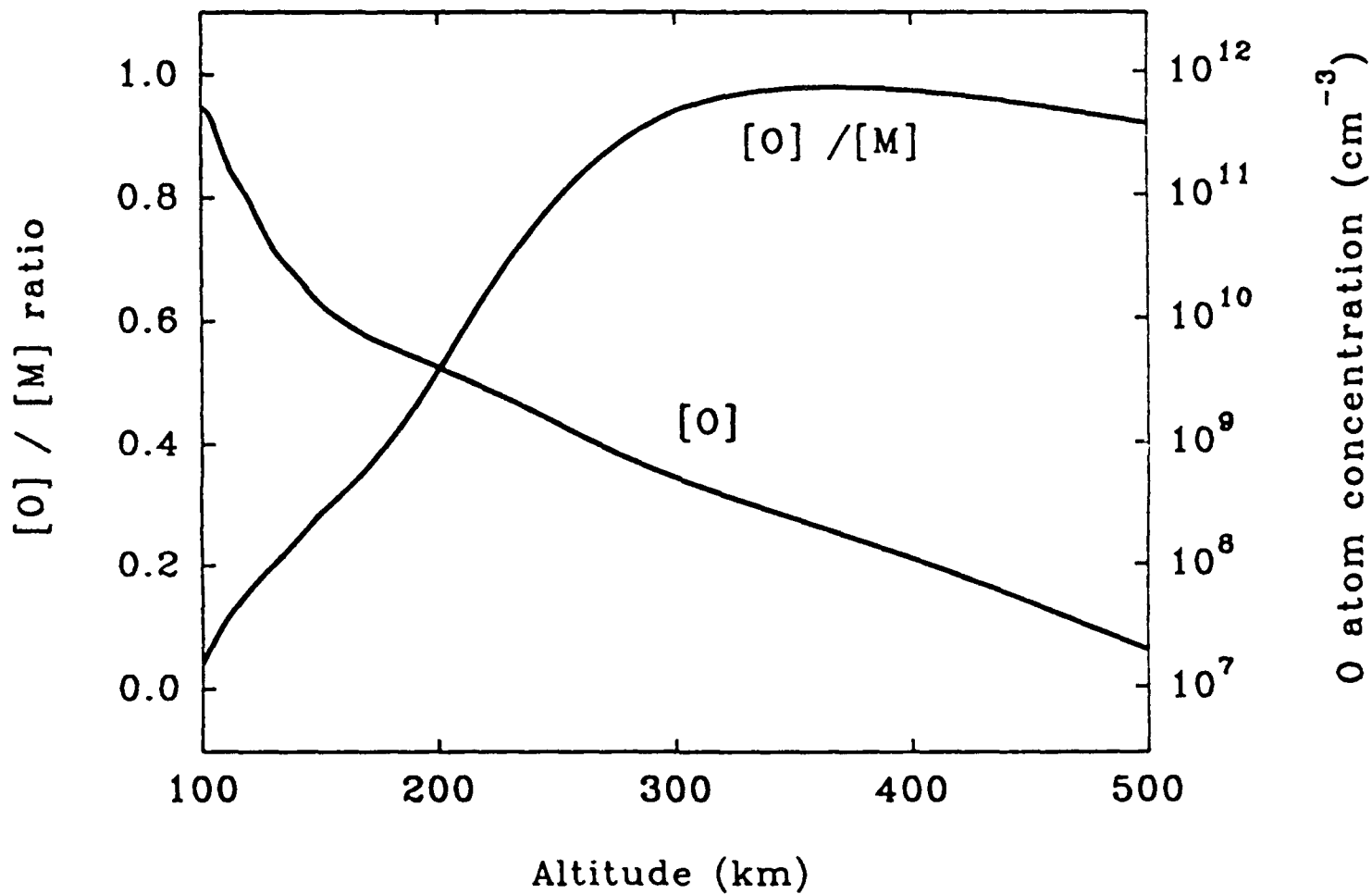# Altitude Dependence
H_2O / O atom interaction

Figure 10. O atom concentration and mixing ratio as a function of altitude.

where V_{th} is the thermal velocity of the outgassed molecules, i.e., the velocity of the molecules with respect to the vehicle.

6.3.3 Signal-to-Noise Ratio

6.3.3.1 Signal

The water vapor signal in the single pixel containating the outgassing spacecraft is given by

$$S = I \frac{A}{R^2} \eta \, T \frac{1}{h\nu} t \qquad (counts)$$

where I is the apparant radiant intensity of the water vapor cloud (W sr^{-1}), A is the area of the collection optics (cm^2), R is the range from the sensor to the outgassing spacecraft (cm), η is the detector quantum efficiency, T is the filter transmission, and t is the integration time (sec).

6.3.3.2 Noise Sources

We consider three noise sources for evaluating the detection of outgassed water vapor at low altitudes. Each dominates under different sensor configurations and detection conditions. The detector readout noise is given by

$$N_{readout} = R \cdot \sqrt{n_{frames}} \qquad (counts)$$

where R is the readout noise (assumed to be 100 counts per frame) and n_{frames} is the number of frames integrated.

For sensors operating from low altitudes, radiance from the atmosphere is considered. As an example we assume a sensor altitude of 60 km and a 45° zenith angle. The atmospheric radiance at 2.8 μm obtained from LOWTRAN 7 as a function of sensor altitude is listed in Table 5. At 1.5 μm, the atmospheric radiance is dominated by the radiance from the airglow layer at 90 km (7.0E(-8) W cm^{-2} sr^{-1} μm, 45° zenith angle).

Table 5

2.8 μm Atmospheric Spectral Radiance (Slant Path to Space, 45° Zenith Angle)

Sensor Altitude (km)	Spectral Radiance (w cm^{-2} sr^{-1} μm^{-1}
80	1.4E(-14)
70	2.4E(-13)
60	8.9E(-12)
50	2.2E(-10)

The atmospheric radiance can be discriminated against by using an on-band/off-band filtering technique. The on-band filter detects the narrowband H_2O emission and the broadband background while the off-band filter detects only the broadband background. The background is then subtracted from the signal plus background leaving only the signal plus the fluctuations in the background. Preliminary bandpasses of the on-band filters are 1.4-1.7 μm (OH $\Delta v = 2$) and 2.65-3.25 μm (OH and H_2O $\Delta v = 1$).

The noise in the atmospheric radiance, N_{atmos}, is given by

$$N_{atmos} = [L_{atmos} \; A \; \Omega \; \Delta\lambda \; \frac{1}{h\nu} \; \eta \; T \; t]^{1/2} \quad (counts)$$

where L_{atmos} is the atmospheric spectral radiance (W cm^{-2} sr^{-1} μm^{-1}), Ω is the pixel field-of-view (sr), and $\Delta\lambda$ is the bandwidth of the filter (μm).

During the day, the sunlight reflected from the hardbody itself becomes a noise source for water vapor detection. This broadband background also can be discriminated against by using the on-band/off-band filtering technique. The noise in the reflected sunlight signature, N_{sunlit}, is given by

$$N_{sunlit} = [\frac{1}{\pi} \; E_{solar} \; rA_{HB} \; \Delta\lambda \; \frac{1}{h\nu} \; \frac{A}{R^2} \; \eta \; T \; t]^{1/2} \quad (counts)$$

where E_{solar} is the solar spectral irradiance (W cm^{-2} μm^{-1}), and rA$_{HB}$ is the reflectivity-area of the spacecraft. The corresponding off band filters could be located at 1.1 - 1.4 μm and 2.25 - 2.65 μm. These bands would detect only the daytime hardbody reflection. The grey-body radiation at 3 μm is quite small.

To obtain the total noise contribution, the components are added in quadrature.

$$N_{total} = [N^2_{readout} + N^2_{atmos} + N^2_{sunlit}]^{1/2} \quad (counts)$$

6.3.3.3 Signal-to-Noise Ratio Range Dependence

The signal-to-noise ratio has an unusual range dependence. At night, the dominant noise will be the detector readout noise or the atmospheric radiance. Neither noise term has a dependence on target range

$$N_{read} \neq f(R)$$

$$N_{atm} \neq f(R)$$

Under sunlit conditions, the noise may be dominated by the fluctuations in the hard body signature. The signature itself is inversely proportional to the square of the range, therefore the fluctuations in that signature are inversely proportional to the range

$$N_{sunlit} \propto \frac{1}{R}$$

The total noise is obtained by adding the individual sources in quadrature

$$N_{total} \propto [N^2_{readout} + N^2_{atmos} + N^2_{sunlit}]^{1/2}$$

If the radiating H_2O cloud is obtained within a single pixel, then the signal in that pixel is dependent on the inverse square of the range

$$S_{small} \propto \frac{1}{R^2}$$

When the radiating H_2O cloud has expanded outside of a single pixel, then the single pixel signal is independent of range

$$S_{large} \neq f(R)$$

The signal-to-noise range dependence is summarized in Table 6.

Table 6

Signal-to-Noise Range Dependence

	$r_{cl} <$ Footprint	$r_{cl} >$ Footprint
Dark	$S/N \propto 1/R^2$	$S/N \neq f(R)$
Sunlit	$S/N \propto 1/R^2$ or $S/N \propto 1/R$	$S/N \propto R$ or $S/N \neq f(R)$

6.4 High Altitude H_2O Emissions

6.4.1 Excitation Mechanisms

At high altitudes, the O atom concentration decreases; therefore, additional excitation mechanisms must be invoked to calculate water vapor signatures. We have evaluated the H_2O emission at 6.3 microns for high altitude (Z > 500 km) spacecraft. There are two mechanisms that result in water vapor emission at 6.3 μm: resonance scattering of earthshine and thermal excitation (self- emission). Each mechanism is present both at night and during the day.

Table 7 lists the fundamental infrared transitions of water, when τ_{Rad} is the radiative lifetime of the upper state, B is the Einstein coefficient for stimulated absorption, f is the dominant spectral flux (earthshine at 6.3 μm, sunshine at 2.7 μm). The excitation rate (and emission rate) is obtained by multiplying the Einstein B coefficient by the spectral irradiance (B·f).

Table 7

Fundamental Infrared Transitions of Water

Transition	λ (μm)	τ_{rad} (ms)	B (m² Hz J⁻¹)	f (W m⁻² Hz⁻¹)	B·f (s⁻¹)
010←000	6.27	44.3	1.12E(9)	1.31E(-12)	1.47E(-3)
001←000	2.66	11.8	3.19E(8)	1.13E(-12)	3.61E(-4)
100←000	2.73	121	3.38E(7)	1.07E(-12)	3.61E(-5)

Thermal excitation is simply the self emission from the outgassed water vapor. The water molecules' rotation-vibration state distribution is related to the temperature of the spacecraft. The relationship between the spacecraft apparent temperature and the water vapor vibrational temperature is not straightforward. However, if the spacecraft vehicle internal structure itself is not covered with insulation, the vibrational temperature is probably close to the apparent temperature of the vehicle. If the spacecraft is covered with MLI, the apparent temperature of the vehicle is cold. The vehicle itself, however, may still be quite warm. The water vapor vibrational temperature will lie somewhere between the vehicles actual surface temperature and the apparent spacecraft temperature (temperature of the outside MLI layer).

The population of the $v_2 = 1$ vibrational state is given by

$$P(v_2=1) = \frac{1}{q} \cdot e^{hv_i/kt}$$

The water vapor vibrational partition function, q, is given by

$$q = \prod_{i=1}^{3} \frac{1}{1 - e^{-hv_i/kT}}$$

For water vapor at the temperatures of interest $q \approx 1$. Table 8 lists the $v_2 = 1$ population as a function of temperature.

Table 8

H_2O $v_2 = 1$ Population as a Function of Temperature

Temperature (°K)	$P(v_2 = 1)$
300	4.9E(-4)
280	2.8E(-4)
260	1.5E(-4)
240	7.3E(-5)
220	3.1E(-5)

6.4.2 Water Vapor Cloud Brightness

6.4.2.1 Resonance Scattering

The apparent radiant intensity of the water vapor cloud due to resonance scattering at 6.3 μm is given by

$$I = \frac{1}{4\pi} B \cdot f N_{H_2O} hv \quad (W/sr)$$

where N_{H2O} is the number of H_2O molecules in the pixel field-of-view. At altitudes where the LWIR mechanisms dominate (Z > 500 km), the water vapor cloud will be large compared to the pixel footprint.

The number of water molecules in the sensor field-of-view is calculated by first integrating the water concentration along the line-of-sight to obtain a column density. That

43

column density is then integrated over the pixel footprint. The column density of water observed by a detector viewing along a line-of-sight displaced a distance, c, from an outgassing object is given by

$$[H_2O]_{column} = \int [H_2O] \, (z) \, dz$$

$$= 2\pi \int [H_2O]_o \, r_o^2 \, \frac{dz}{(z-R)^2 + c^2}$$

$$= \pi \, [H_2O]_o \, \frac{r_o^2}{c} \qquad (molecules \ cm^{-2})$$
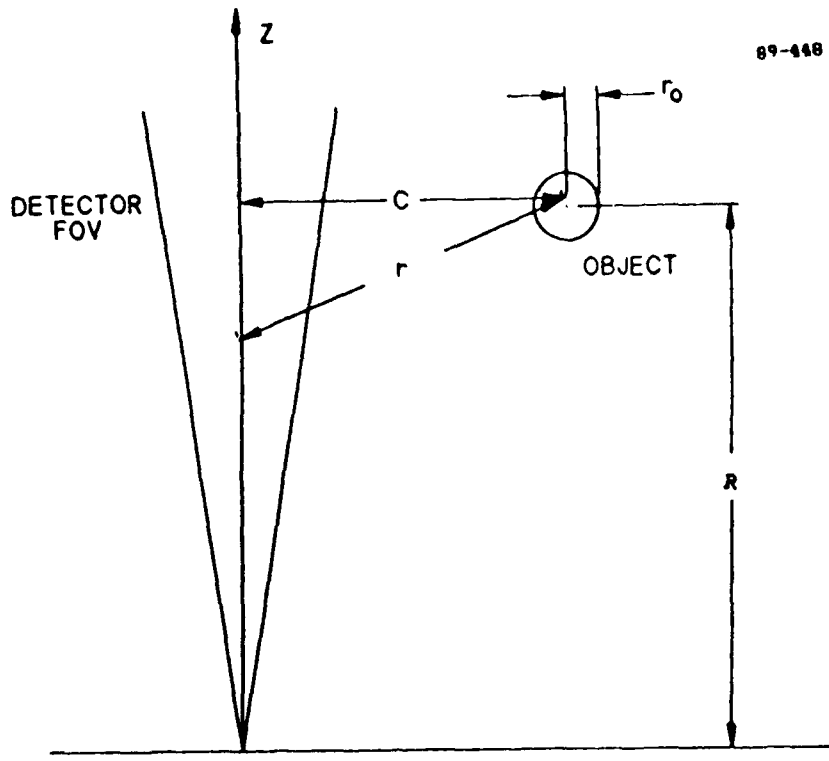
where R is the distance from the sensor to the object (see Fig. 11). To calculate the number of molecules in the pixel field-of-view, the column density is integrated over the pixel footprint (Figure 12).

$$NH_2O = \int \pi \, [H_2O]_o \, \frac{r^{o2}}{c} \, 2\pi c \, dc$$

$$= \pi^2 \, [H_2O]_o \, r^{2 \cdot} \, \sqrt{\Omega} \, R \qquad (molecules)$$

6.4.2.2 Thermal Emission
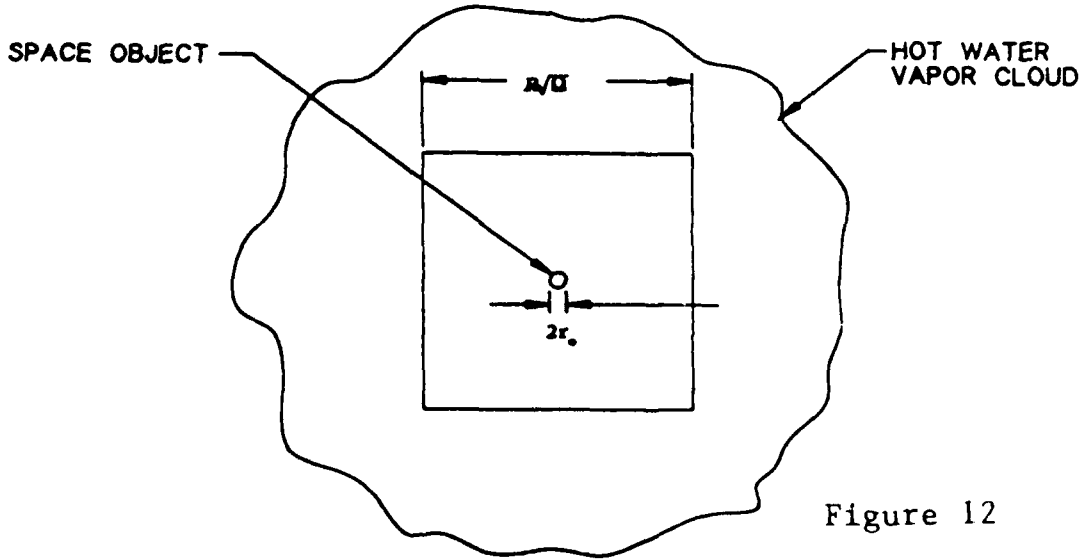
The apparent radiant intensity of the water vapor cloud due to thermal emission at 6.3 μm is given by

$$I_{thermal} \approx \frac{1}{4\pi} \int P(\nu_2=1) \, \frac{1}{\tau_{rad}} \, [H_2O]_o \, \frac{r_o^2}{r^2} \, e^{-r/vt} \, h\nu \, 4\pi \, r^2 \, dr$$

$$= P(\nu_2=1) \, [H_2O]_o \, r_o^2 \, h\nu \, v \, [\exp(-r_o/v\tau_{rad}) - \exp(-\sqrt{\Omega}R/2v\tau)]$$

44
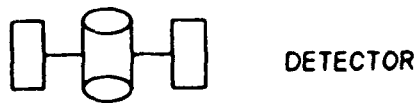
Figure 11

Figure 12

Figure 11 & 12.   The water vapor cloud is large compared to the pixel footprint. (11) First the column density is calculated by integrating along a line-of-sight displaced to a distance, c, from the object. (12) Then the column density is integrated around the object out to the pixel boundary thereby yielding the total amount of H_2O in the pixel field-of-view.

45

where $P(v_2=1)$ is the population of the $v_2 = 1$ vibrational level, τ_{Rad} is the radiative lifetime of the $v_2=1$ vibrational state, and v is the thermal velocity. The exponential factor accounts for the decrease in emission probability with distance from the outgassing object. The model is approximate (see Fig. 13) in that there are regions that are not integrated; however, because the radiative lifetime is relatively short, the integral does converge rapidly with increasing field-of-view.

6.4.3 Signal-to-Noise Ratio

6.4.3.1 Signal

The water vapor signal in the single pixel contaminating the outgassing spacecraft is given by

$$S = (I_{RS} + I_{therm}) \frac{A}{R^2} \eta \, T \, \frac{1}{h\nu} \, t \qquad (counts)$$

where I_{RS} is the apparent radiant intensity of the water vapor cloud due to resonance scattering and I_{therm} is the apparent radiant intensity due to water vapor thermal self-emission.

6.4.3.2 Noise Sources

We have considered two noise sources for evaluating the detection of outgassed water vapor at high altitudes. Each dominates under different sensor configurations and detection conditions. The detector readout noise is assumed to be 100 counts frame^{-1}.

$$N_{readout} = 100 \qquad (counts \, frame^{-1})$$

In addition, the fluctuations in the greybody emission from the spacecraft itself are a noise source for water vapor detection. In fact, the greybody emssion is 100-1000 times more intense than the H_2O emission at 6.3 μm. This broad band background may be discriminated against by using the on-band/off-band filtering technique discussed previously. The preliminary bandpass of the on-band filter is 5.8-6.8 μm. The off-band filter transmits 5.3-5.8 μm and 6.8-7.3 μm. By straddling the emission band, the variation in the slope of the blackbody emission curve with temperature is taken into account. In this manner, the greybody emission can be

THERMAL EXCITATION INTEGRAL
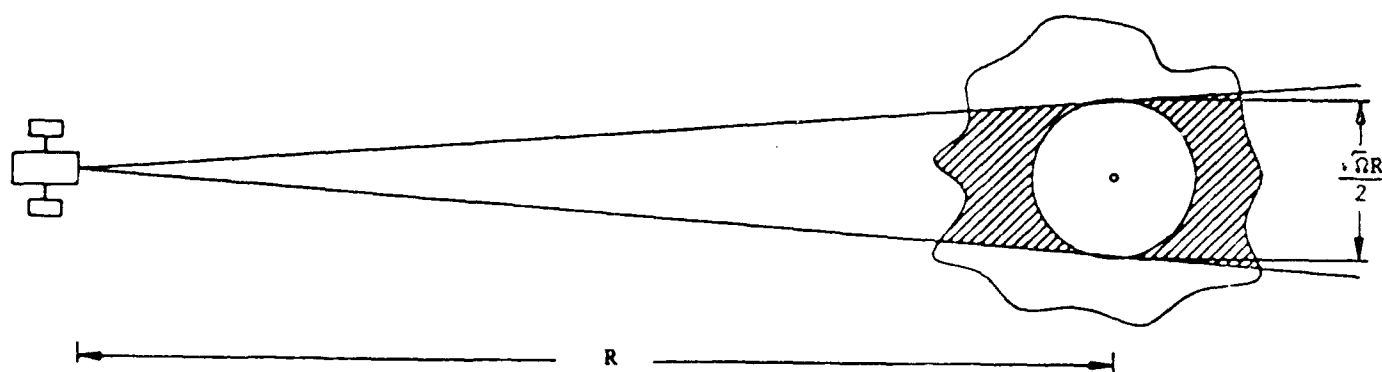

Figure 13. Integration of the apparent radiant int..isity due to water vapor thermal emission. The integral is approximate in that there are regions that are not integrated; however, the integral coverges rapidly with increasing field-of-view.

subtracted better regardless of the spacecraft's apparent temperature. The noise from the greybody emission, N_{GB}, is given by

$$N_{GB} = \left[\frac{1}{\pi} E_{GB} \, \epsilon A_{HB} \, \Delta\lambda \, \frac{1}{h\nu} \, \frac{A}{R^2} \, \eta \, T \, t \right]^{\frac{1}{2}}$$

where E_{GB} is the blackbody spectral surface irradiance (Watts cm^{-2} μm^{-1}), ϵA_{HB} is the emissivity-area of the spacecraft. To obtain the total noise contribution, the components are added in quadrature.

$$N_{total} = \left[N_{readout}^2 + N_{GB}^2 \right]^{\frac{1}{2}}$$

6.5 H₂O Emissions Signal-to-Noise Evaluation

To evaluate the importance of H_2O emissions, we have calculated signal-to-noise ratios for a typical size SWIR and LWIR sensor.

6.5.1 Low Altitude H₂O Emissions

The water vapor single pixel apparent radiant intensity depends upon the sensor parameters - the outgassed cloud may be smaller or larger than the pixel footprint. As an example of typical values, Table 9 lists water vapor apparent radiant intensities at 3 μm for a typical size sensor observing the water vapor cloud surrounding a 7 km sec^{-1} spacecraft. Since the 3 μm emission is brighter than the 1.5 μm emission, and the reflected sunlight is more significant at 1.5 μm, our evaluation concentrates on the 3 μm emissions. Table 10 lists the water vapor detection signal-to-noise ratio for a typical size sensor observing the water vapor cloud surrounding a 7 km sec^{-1} spacecraft. The total integration time is 0.5 sec; i.e., 15 samples at a 30 Hz frame rate.

The apparent radiant intensities listed in Table 9 show an unusual altitude dependence; i.e., the apparent radiant intensity first increases, then decreases, with increasing altitude. If the water vapor cloud is contained within a single pixel, the apparent radiant intensity is proportional to both the O atom concentration and the mean free path. The mean free path, in turn is

48

Table 9

H$_2$O Apparent Radiant Intensities
for a Typical Size SWIR Sensor Observing Outgassing From
a 7 km sec^{-1} Spacecraft

Range = 300 km	
Altitude (km)	3 μm (W/sr)
150	0.078
175	0.11
200	0.15
250	0.045
300	0.064

inversely proportional to the total density ($[N_2] + [O] + [O_2]$); therefore, the radiant intensity is proportional to the mixing fraction of [O]. The radiant intensity will therefore increase with increasing altitude until either, (1) the cloud expands outside of a single pixel, or (2) O atoms become the dominant atmospheric species (Z > 250 km).

The curious range dependence of the signal-to-noise ratio is also evident in Table 10. At 125 km altitude, the H_2O cloud radiation is contained within a single pixel. The signal will have a $1/R^2$ dependence. At night, the detector readout dominates the noise, and the S/N shows a $1/R^2$ dependence. Under sunlit conditions, the fluctuations in the hardbody signature dominate the noise, and the S/N shows a $1/R$ dependence. At 250 km altitude, the radiating H_2O cloud has extended outside of the pixel footprint. The single pixel signal will be independent of range. At night, where the readout dominates the noise, the S/N is independent of range. Under sunlit conditions, where these fluctuations in the hardbody signature dominate the noise, the S/N actually increases with range.

6.5.2 High Altitude Emissions

The H_2O apparent radiant intensities predicted at high altitudes (Z > 500 km, resonance scattering and self-emission) are much weaker than those predicted at low altitudes (Z < 300 km, O atom interactions). The thermal emission of the spacecraft also provides an intense background against which the weaker H_2O emissions must be detected.

The high altitude H_2O apparent radiant intensities predicted for a typical size LWIR sensor are listed in Table 11. The corresponding signal-to-noise ratios are listed in Table 12.

6.6 Summary and Conclusions

Laboratory and field data indicate that spacecraft covered with ablative heat shielding or MLI will outgas water vapor for long times. Recent laboratory and field measurements also suggest that the interaction of this outgassed water vapor with the ambient atmosphere produces readily measurable NIR and SWIR emissions. At high altitudes, where the atmospheric interaction is reduced, other mechanisms produce LWIR emissions.

We have modeled the evolution of the outgassed water vapor cloud, the resulting NIR, SWIR, and LWIR emissions, and the response of two typically dimensioned sensors to these emissions. Readout noise and atmospheric radiance are taken into account. In addition, the

Table 10

Water Vapor Signal-to-Noise
Ratio for a Typical Size Sensor
Observing Outgassing From a 7 km/s Spacecraft

RV Altitude (km)	Night 3 μm (S/N)	Sunlit 3 μm (S/N)
Range = 100 km		
150	1700	170
200	310	31
250	31	3
300	4	1
Range = 300 km		
200	310	55
250	31	9
300	4	1
Range = 500 km		
250	31	14
300	4.4	2

Table 11

H₂O Apparent Radiant Intensities for a
Typical Size LWIR Sensor Observing Outgassing From
a High Altitude Spacecraft

Range (km)	S/N
Temperature = 220° K	
100	27
300	26
1000	21
Temperature = 300° K	
100	14
300	10
1000	8

Table 12

H₂O Signal-to-Noise Ratios for a Typical
Size LWIR Sensor Observing Outgassing From
a High Altitude Spacecraft

RV Range (km)	RS (mW/sr)	Therm (mW/sr)
T = 220° K		
100	1.5	0.078
300	4.4	0.094
1000	15	0.094
T = 300° K		
100	1.5	1.4
300	4.4	1.8
1000	15	1.8

hardbody emission (reflected sunlight in the SWIR or greybody emissions in the LWIR) become noise sources for water vapor measurement. The LWIR H_2O emission intensity is 100 - 1000 times less than the greybody signature.

Our signal-to-noise calculations predict that typically dimensioned SWIR and LWIR sensors can measure H_2O emissions surrounding spacecraft. The emissions due to atmospheric interactions (Z < 300 km) are much stronger than those due to resonance scattering and self-emission (Z > 500 km) for high velocity vehicles. The atmospheric velocity dependent, while the high altitude mechanisms are not.

7.0 ANALYSIS OF HIGH ALTITUDE ATMOSPHERIC EMISSIONS AT HIGH DOSING LEVELS

The results of our efforts during this time period are summarized in two papers which have been presented at several conferences. The first paper, "Excited State Distributions from Artificial Aurora Produced by the EXCEDE III Experiment", was presented at the meeting of the IRIS Specialty Group on Targets, Backgrounds, and Discrimination in Albuquerque, NM, 29-31 January 1991. This paper was the basis for presentations at the Fall 1990 and Spring 1991 Meeting of the American Geophysical Union[15] and at the 1991 Cambridge Workshop in Theoretical Geoplasma Physics - Nonlinear Phenomena and Active Experiments which were attended by Dr. R.J. Rieder and Dr. R.L. McNutt. Unfortunately because of security clearance difficulties the paper was able to be presented only at the Cambridge Workshop.

Data analysis from the x-ray experiment was started during this period and is still ongoing. The results are being written up for rapid publication in Geophysical Research Letters and is close to being ready for submission. A draft of the paper, "Remote X-Ray Measurements of the Electron Beam from the EXCEDE III Experiments" is included in Appendix A. The experiment consisted of two detectors, one having a large area (18 cm^2) and the other having a small area (2 cm^2) for the purpose of expanding the dynamic range of the experiment. The objective of the experiment was to make remote measurements of the beam energy by detecting and characterizing the bremsstrahlung radiation emitted by the beam electrons. This paper was the basis for presentations at the Spring 1991 Meeting of the American Geophysical Union and at the 1991 Cambridge Workshop in Theoretical Geoplasma Physics -Nonlinear Phenomena and Active Experiments.

8.0 REFERENCES

1. J. Meeus, "Astronomical Formulae for Calculators" Willmann-Bell, Richmond, VA (1982).
2. E. Murad et al., "Visible Light Emission Excited by Interaction of Space Shuttle Exhaust with the Atmosphere", Geophys. Res. Lett., 17, 2205 (1990).

3. B.L. Upschulte et al., "Laboratory Measurements of IR Cross-Sections from Fast O-Atom Collisions", (preprint 1990).

4. F.C. Witteborne et al., "Nighttime Spectroscopic and Photometric Observations of Spacelab 2 and Other Satellites", (preprint 1985).

5. J.B. Elgin et al., "Modeling of Atmospherically-Induced Gas Phase Optical Contamination from Orbiting Spacecraft", (preprint 1990).

6. E. Murad et al., "Collisions of Space Shuttle Exhaust with the Atmosphere - Effects of Orientation", (preprint 1990).

7. D. Coe et al., MIT/Lincoln Lab have measured MLI outgassing rates.

8. A.P.M. Glassford and C.K. Liu, J. Vac Sci. Tech., 17, 694 (1980); Glassford has performed outgassing measurements on many spacecraft materials.

9. E. Zipf, University of Pittsburgh, has measured outgassing rates of phenolics and MLI films.

10. A.P.M. Glassford, J. Spacecraft, 7, 1464 (1970).

11. A.P.M. Glassford et al., J. Vac. Sci. Tech., A2, 1370 (1984).

12. E.A. Albers et al., "Absolute Measurements of Rate Coefficients for the Reaction of H and O Atoms with H_2O_2 and H_2O", Proc. 13th Int'l. Sympos. on Combustion, pp 81-88, (1971).

13. G.N. Freeman et al., "Composite High Altitude Radiation Model (CHARM), Vol: Code Development", AFAL-TR-87-019 (1987).

14. P. Bernhardt, "High Altitude Gas Release: Transition from Collisionless Flow to Diffusive Flow in a Nonuniform Atmosphere", J. Geophys. Res., 84, 793 (1979).

15. EOS Transactions, American Geophysical Union, Spring Meeting 1991, Vol. 72, No. 17, April 23, 1991/Supplement, p. 215.

Appendix A

Remote X-Ray Measurements of the Electron Beam
From the EXCEDE III Experiment

REMOTE X-RAY MEASUREMENTS OF THE ELECTRON BEAM FROM THE EXCEDE III EXPERIMENT

S. A. Rappaport, R. J. Rieder, W. P. Reidy,
R. L. McNutt, Jr., and J. J. Atkinson

Visidyne, 10 Corporate Place, South Bedford Street, Burlington, MA

D. Paulsen

PL/GP/OPB, Hanscom AFB, MA

Abstract. The EXCEDE III rocket experiment successfully produced an artificial aurora on April 27, 1990 with an 18 A beam of ~2.4 keV electrons. The experiment consisted of an accelerator module and a sensor module in a mother-daughter configuration. The beam was fired along the Earth's magnetic field lines between the altitudes of ~62 and 115 km during the flight. A major concern prior to the flight was that the injection of such an overdense electron beam into the lower ionosphere would charge the accelerator module to a significant fraction of the beam potential. To monitor the primary electrons remote from the rocket, two X-ray proportional counters were included as part of the sensor module. X-ray spectra from bremsstrahlung emission yield a direct measure of the primary electron beam energy outside the plasma sheath surrounding the accelerator module. Analysis of these spectra show that a hard upper limit on the accelerator module potential is ~200 V for the entire time that the beam was on, assuming no loss by attenuation or through beam-plasma interactions. We also find that the X-ray intensity was modulated at the few percent level by firings of the attitude control jets.

Introduction

EXCEDE III (Excitation by Electron Deposition) is an atmospheric energy deposition rocket experiment that was launched on April 27, 1990 from the White Sands Missile Range (WSMR) [Paulsen et al. 1991]. This flight is the most recent in a series of such experiments [e.g., O'Neil et al., 1978a,b; 1982]. An artificial aurora was successfully produced between the altitudes of ~62 and 115 km by an electron beam with a primary electron energy of ~2.4 keV

and current of 18 Amperes. The electron beam was fired along the geomagnetic field lines which have an elevation angle of 61.1° with respect to the local horizontal at WSMR.

EXCEDE III was configured as a mother-daughter experiment. One section contained the electron accelerator and associated instrumentation, while the other section carried sensors for spectral and spatial measurements. There were 22 optical instruments which covered the spectral region from 0.18 microns to 25 microns, 2 video cameras, and 5 film cameras. In addition, the instrumentation included an electrostatic analyzer, a retarding potential analyzer, an atomic oxygen experiment, and 2 X-ray detectors covering the band from 1-10 keV. Twenty-six beam firing cycles were studied, each cycle consisting of 4.73 seconds with the beam on and 2.37 seconds with the beam off. We report here on remote measurements made from the sensor module of the bremsstrahlung X-ray emissions from the electron beam. To our knowledge, this is the first measurement of its kind to be carried out in space.

Bremsstrahlung X-Ray Experiment

The X-ray detectors were one of eight experiments provided by Visidyne and consisted of two proportional counters filled with 800 Torr of Ar (90%) and CO_2 (10%) and sealed with 25 μ thick Be windows. The unobstructed areas of the windows for the detectors were 2 cm^2 and 18 cm^2, respectively. The different detector areas were used to expand the dynamic range of the experiment. The quantum efficiency of the detectors was ~90%, 45%, 60%, 40% and 6% at energies of 4, 3, 2, 1.5 and 1 keV, respectively; the rapid decline toward low energies is due to photoelectric absorption in the windows. The energy resolution of the proportional counters was 18% FWHM at 5.9 keV, and scales approximately as $E^{-1/2}$, where E is the X-ray energy. The field of view of the X-ray detectors was defined by a hexagonal aluminum honeycomb collimator to be 8° (FWHM).

The EXCEDE III experiment timeline was as follows: (1) The sensor module separation occurred at time after launch t = 112 s and at an altitude h = 82 km; (2) the third electron gun cycle (the first for which we have good X-ray data) was at t = 136 s and h = 99 km; (3) the peak altitude

occurred at t = 195 s and h = 115 km; and (4) gun cycle number 23 (the last which yielded good X-ray data) was at t = 278 s and h = 82 km. The sensor module was pushed away from the accelerator payload with a separation velocity of 3.17 m s^{-1} in a direction roughly perpendicular to the electron beam. At the time of the third gun cycle, the separation between the two modules was 76 m, and this distance had increased to 530 m by the time of the 23rd gun cycle. Throughout most of the flight, the field of view of the X-ray detectors was oriented ~28° from the line joining the sensor and accelerator modules, in such a direction so as to intersect the electron beam at a distance from the accelerator module of $\leq$ 0.1 times the practical range of the primary electrons. The 8° field of view of the X-ray detectors always completely covered the electron beam in the transverse direction (across the beam), but included only a portion of the beam equal in length to ~ s × tan 8°, where s is the separation between the sensor and the electron beam. During the 21 gun cycles observed with the X-ray detectors, the length of the electron beam (approximately equal to the practical range of the primary electrons) increased from ~500 meters near gun cycle 3 to ~6 km at apogee, and then decreased again as the payload descended. Correspondingly, the field of view of the X-ray detectors included a few percent of the electron beam during gun cycle 3, a progressively smaller fraction of the electron beam as the payload approached apogee, and a larger fraction of the beam as the payload descended and the separation s increased. By gun cycle 23, virtually the entire electron beam could be covered by the field of view of the X-ray detectors.

X-ray pulse height spectra were accumulated for 1/6 second and telemetered to the ground with 128 pulse-height channels, each of width ~0.08 keV. In addition, there was a "photometer" output mode in which the number of detected X-rays, regardless of energy (over the range ~1-10 keV), were integrated for 20 ms and telemetered to the ground. This latter mode had better temporal resolution than the pulse height mode, but essentially no spectral information.

Data and Analysis

In all, ~600 pulse-height spectra were recorded from each detector during the flight. A sample spectrum containing a total of ~2000 X-ray events is shown in Figure 1. Under

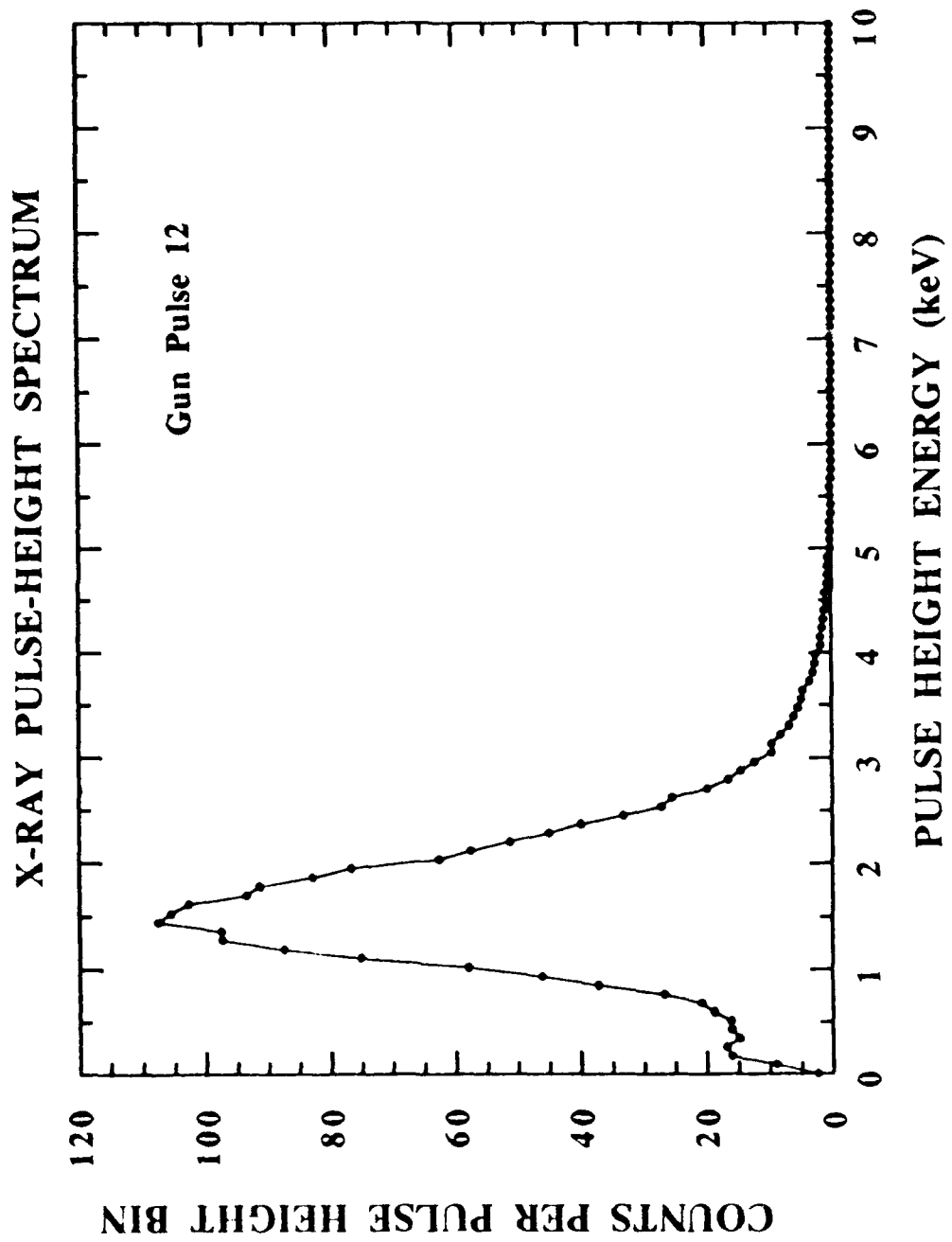# X-RAY PULSE-HEIGHT SPECTRUM

Gun Pulse 12

Figure 1. Pulse height spectrum from the larger-area X-ray proportional counter. The spectrum displayed is an average of 15 spectra recorded during gun cycle 12.

normal operating conditions, the pulse height distribution of a narrow line source is approximately Gaussian in shape; however, at the high counting rates experienced during the flight (1.5×10^4 s^{-1} to 1.8×10^5 s^{-1} in the large area detector) the pulse height distributions develop a broad, high-energy tail (of relatively small amplitude) and some distortion at low energies. Laboratory calibrations indicate that the centroid of the distribution is not significantly affected by count rates in the range encountered during most of the flight.

To mitigate against any detrimental effects of high counting rates, the analyses and figures presented in this work utilize data from both detectors. We used the data acquired with the large area detector for gun cycles 7 through 18, while for earlier and later gun cycles we used data from the smaller area detector (factor of ~9 smaller than the larger area detector).

The expected thin-target bremsstrahlung X-ray (number) spectrum for electrons of energy E_e is given by (see, e.g., Chap 20, Fig. 1.3b of Evans [1972]):

$$S(E) = S_0 E^{-1} \qquad \text{for } E \leq E_e \qquad (1)$$

$$= 0 \qquad \text{for } E > E_e$$

where S_0 is a constant. For a spectral distribution of electron energies, the resultant bremsstrahlung X-ray spectrum will obviously be more complex than that represented by equation (1). The relatively poor energy resolution of the proportional counters in this low-energy range, however, does not warrant an attempt to fit the data to a more complicated spectrum than the one given in equation (1). We therefore restricted our efforts to determining the single parameter, E_e, under the assumption that the portion of the electron beam under observation at any particular time contains mostly monoenergetic electrons of energy E_e.

For electron energies in the range of ~1.5-3 keV, this type of spectrum (eq. [1]) produces a relatively narrow pulse height distribution in a conventional proportional counter. This results from the fact that the X-ray spectrum is rising rapidly toward low energies, while the corresponding quantum efficiency of the detector is dropping rapidly. The finite energy resolution of the proportional counters broadens this peak into a pulse height

spectrum of the form shown in Fig. 1. The position of the centroid of the pulse height spectrum can then be used to make a direct estimate of the energy of the primary electrons in the beam.

In order to establish the relation between the peak of the pulse height spectrum and the parameter E_e, we carried out extensive simulations of the response of the EXCEDE III proportional counters to bremsstrahlung spectra that result from a variety of primary electron beam energies. First, we computed the expected pulse height distribution that would be recorded by the proportional counter from an input bremsstrahlung spectrum of the form given by equation (1). This was accomplished by convolving the product of the spectrum and the detector quantum efficiency with the detector energy-resolution function. For each such calculation, the energy corresponding to the centroid of the pulse height spectrum was recorded. These calculations were repeated for a wide range of electron (beam) energies. From our simulations, we find that the position E_c of the centroid of the pulse height spectrum is related to the energy of the primary electrons E_e by:

$$E_c \text{ (keV)} \approx 0.4\, E_e \text{ (keV)} + 0.6 \text{ keV} \tag{2}$$

For simplicity we approximated the measured pulse height spectra with a Gaussian distribution and fit such a function to each of the ~600 recorded spectra. Because of the obvious deviations from a simple Gaussian at both large and small pulse heights (see Fig. 1), we restricted the fits to the center 20 channels of each pulse-height distribution. From each of these fits, we extracted the mean pulse height ($\propto E_c$), an intensity ($\propto$ X-ray flux), and the rms width of the distribution. A plot of the relative intensity of the X-ray flux, as measured by the larger-area proportional counter (for gun cycles 7 through 18) and the smaller-area detector (for all other cycles), as a function of time is shown in Figure 2. Each gun cycle firing is indicated along the abscissa. Note the erratic behavior of the electron guns during the first 3 gun pulses. Temporary drops in electron beam current (due to load faults on the gun modules) can be seen in gun cycles 5 and 6. During gun cycles 13 and 14 the current dropped because one of the four gun modules turned off. The anomalous intensity profile of gun cycle 22 is due to a scanning motion of the sensor module near the
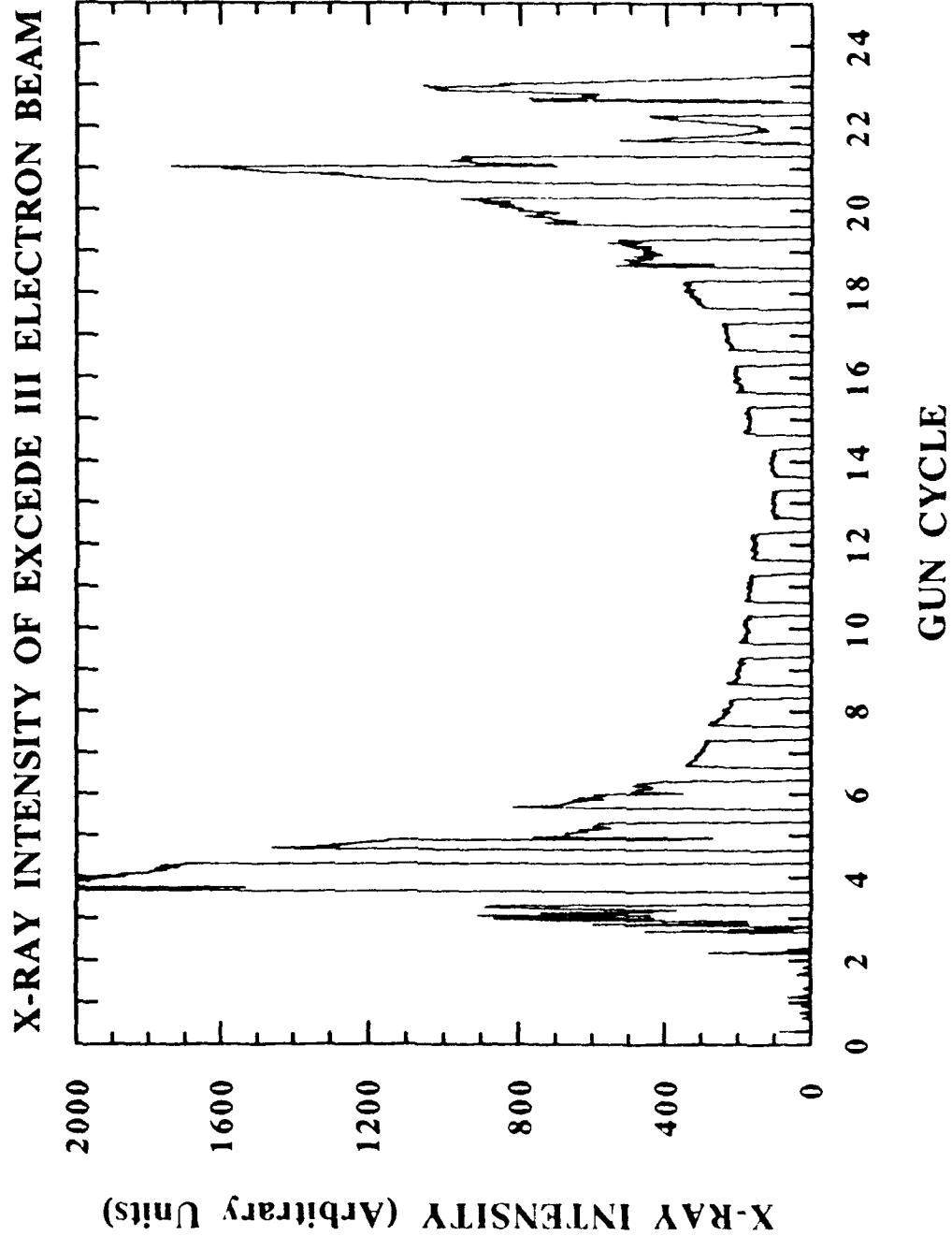
Figure 2. The relative intensity of X-ray emission from the primary electrons in the EXCEDE III beam versus gun cycle during the flight.

63

end of the mission.

The overall X-ray intensity profile seen in Fig. 2, higher near the beginning and end, and lower in the middle of the flight, is due primarily to the changes in atmospheric density with altitude and the concomitant changes in the practical range of the electron beam. At the higher altitudes, the practical range of the electron beam is ~6 km, while at the lowest altitudes represented in the figure, the practical range is only ~100 m. At the higher altitudes the field of view of the X-ray detectors overlaps only a small fraction of the length of the electron beam, and hence the drop off in intensity near apogee. By contrast, at the lower altitudes, the intensity is higher because the field of view of the X-ray detectors overlaps a larger fraction of the length of the electron beam.

For each measured pulse height spectrum we used our fit for the position of the centroid and our laboratory calibration to find the corresponding energy of the centroid (in keV). We then used the energy of the centroid in the pulse height spectrum to estimate the energy of an assumed monoenergetic electron beam (eqn. [2]). A plot of the inferred electron beam energy as a function of gun cycle is shown in Figure 3. We find that the electron energy of the beam during a significant portion of the flight was 2.4 ± 0.2 keV. The erratic behavior of the beam seen at the start of the flight is due to the operating characteristics of the electron accelerator. When a very large current is sensed by the electronics, the accelerator automatically shuts down and attempts to resume operation at a lower voltage. A substantially lower gun voltage is inferred during gun cycle 3 and a smaller step down in voltage is clearly seen in the second half of gun cycle 5. These measurements confirm that a high-energy electron beam propagated away from the accelerator module and that the primary electron energies were substantially as measured at the electron gun.

The intensity of the X-ray emissions also provides a direct measure of the current in the electron beam. In general, the counting rate R in the X-ray detector is related to the beam power P by the following relation:

$$P = 4\pi R \ s \ L \ h\nu/(A_d \ \varepsilon \ \zeta \ \tan\theta) \tag{3}$$

where $\theta = 8°$, A_d is the area of the X-ray detector, ε is the average effective quantum efficiency of the X-ray detector, ζ is the fraction of the energy of a primary electron that is
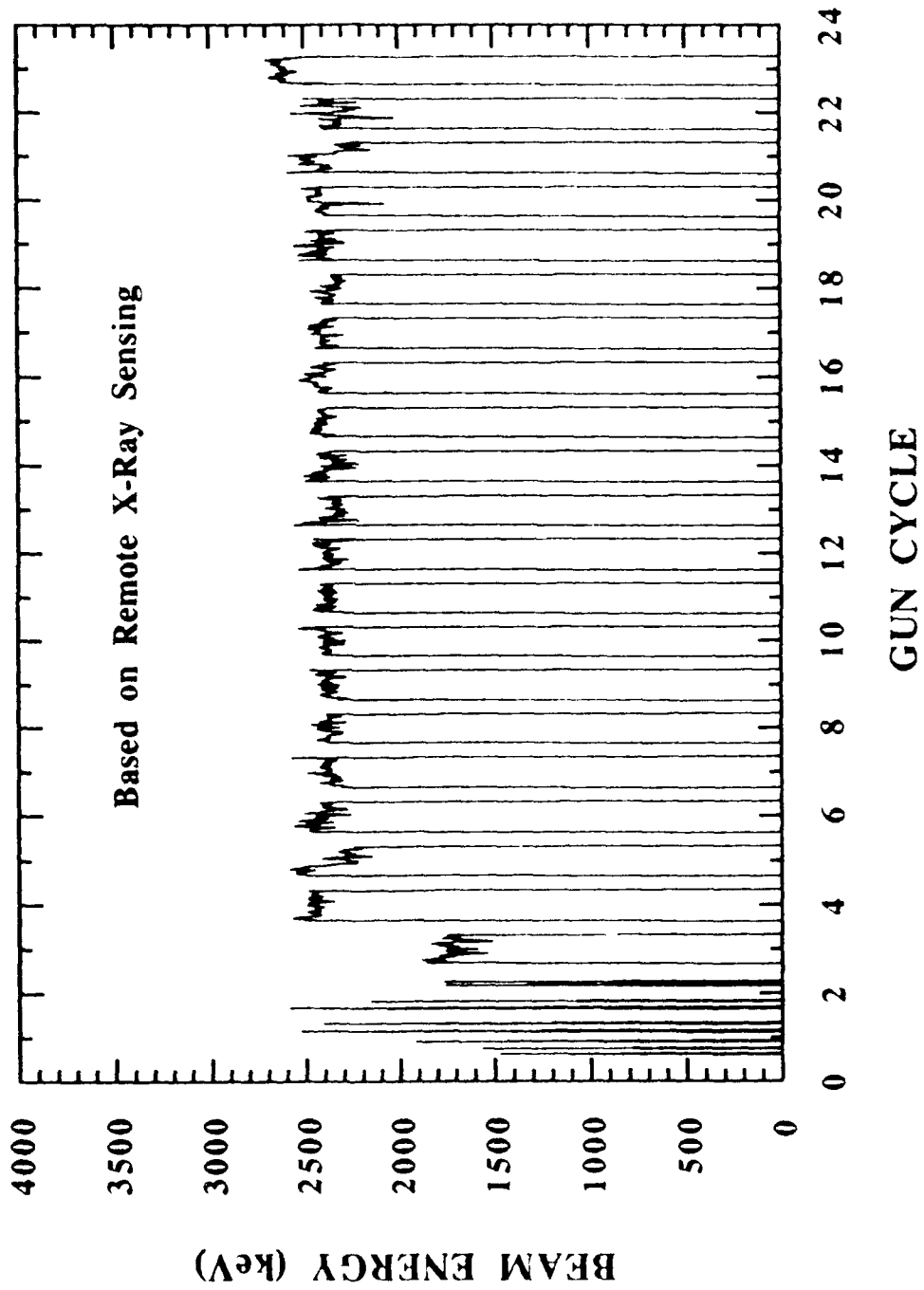
Figure 3. The energy of the primary beam electrons as inferred from X-ray spectra versus gun cycle during the EXCEDE III flight.

ultimately emitted in the X-ray band (see, e.g., Chap. 21, eqn. 2.10 of Evans [1959]), s is the separation between the sensor and accelerator modules, $h\nu$ is the energy of the X-rays and L is the practical range of the electron beam. Equation (3) was evaluated with the appropriate measured parameter values throughout the flight. The average beam power is found to be 48 kW. Since the energy of the primary electrons is ~2.4 keV, this total power indicates a current of ~20 Amperes, in reasonable agreement with the more accurate current measurement of ~18 Amperes made at the electron guns (C. Howlett, private comm.).

Charging of the Accelerator Module

The best estimate of the energy of the electron beam averaged over gun cycles 6 to 20 made from the accelerator module (C. Howlett, private comm.) yields a value of 2.5 ± 0.1 keV. Comparison of this value with that measured remotely (at a distance of many Debye lengths) using the X-ray emission of the primary beam electrons indicates agreement to within the uncertainties of the measurements of ~200 eV. This consistency, in turn, indicates that significant charging of the accelerator module did not occur. If an electron beam is emitted into an underdense plasma (ambient plasma density less than the beam plasma density), and there are no additional sources of charged particles, a return current sufficient to neutralize the vehicle potential may not be available. In such a case, the effective accelerating potential of the electrons can be substantially reduced (and the current density as well, for operation near the perveance limit). In the case of EXCEDE III, there were apparently sufficient sources of charged particles present (due to electron-impact ionization of the ambient neutral species [see, e.g., Winglee, 1990]) that the vehicle floating potential remained small (<200 eV).

Beam Power Oscillations

Searches for temporal periodicities in the X-ray intensity were carried out on the X-ray photometer mode data with 0.020 s time resolution. The data were first passed through a "median" filter of width 0.8 sec. In this filtering scheme, the median value of the X-ray intensity in each 0.8 sec interval is subtracted from the observed signal. This has the effect of reducing the effects of the large changes in X-ray

signal due to the gun on-off cycle and the overall low-frequency intensity variations due to the intercepted fraction of the beam with altitude (See Fig. 2). After filtering, the resultant data set was subjected to a Fourier analysis. The power spectral density obtained from this analysis is shown in Figure 4. Aside from some residual lower-frequency noise below ~2 Hz there is a prominent peak at 11.36 Hz as well as its first harmonic. In addition, there is some evidence for another peak at 12.26 Hz.

These oscillations have been confirmed with most of the other instruments on both the sensor and accelerator modules, including two 3914 boresighted photometers, an electrostatic analyzer, and a retarding potential analyzer. The two oscillation frequencies are the same in the various data sets and can be matched in time to the firing of the nitrogen-emitting gas jets in the Attitude Control System (ACS) on the accelerator module (C. Howlett, private comm.) The amplitude of the oscillations appears to be sensitive to the gas required by a given maneuver. These oscillations, when they are present, minimally impact the primary goals of the EXCEDE III experiment. At the same time, their presence may provide a unique opportunity for further diagnostics which were not originally planned.

Previous experiments have shown that neutralization currents to electron-beam emitting spacecraft are affectd by neutral gas releases [cf. ,e.g., Gilchrist et al., 1990]. A quantitative study of the spectral data used to produce Fig. 3 shows that the time average of the energy of the primary electrons changes by less than ~25 eV between times of oscillations and quiescence. Thus, the oscillations do not appear to be due to modulations in the spacecraft potential of more than ~twice this value or ~50 V.
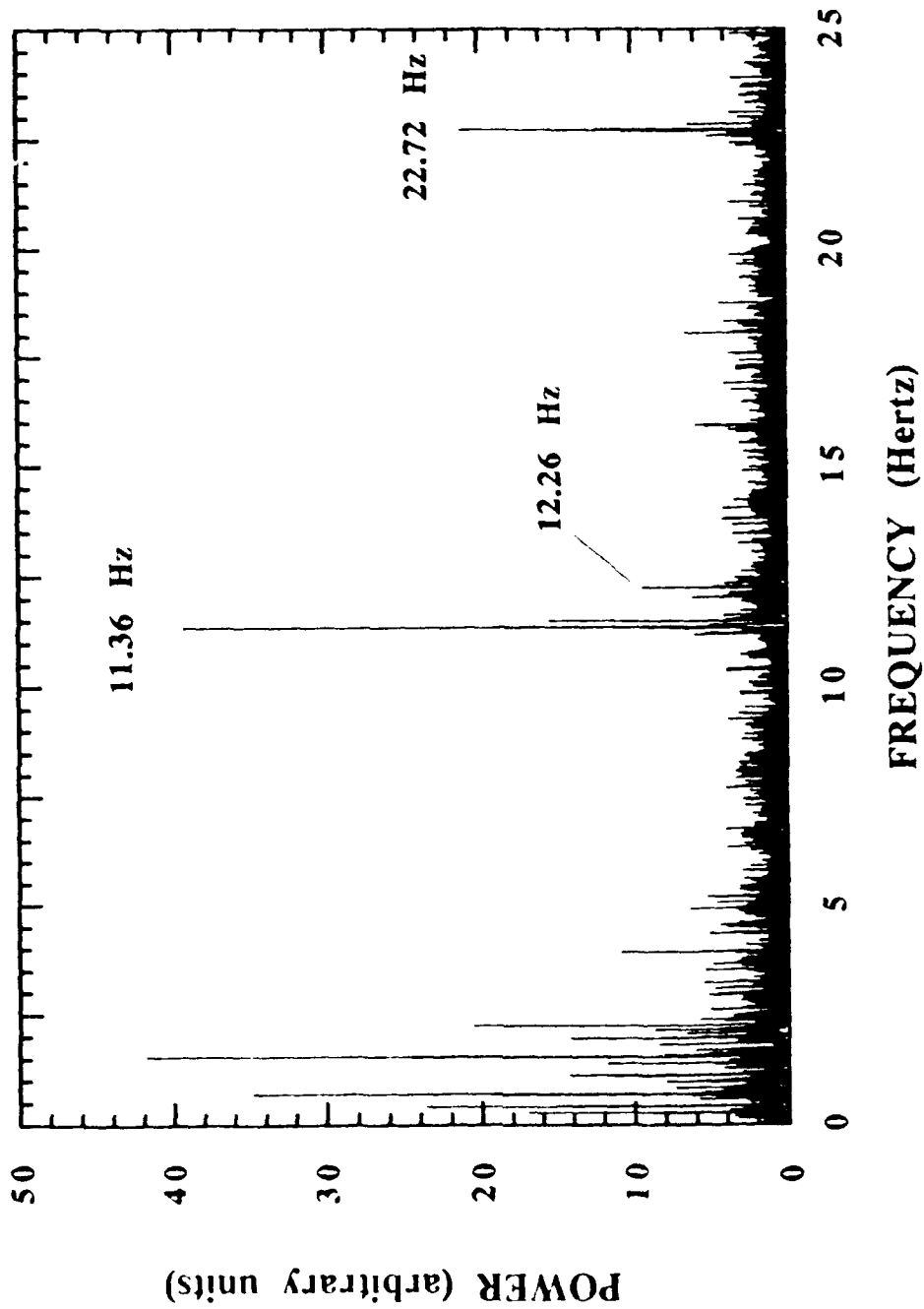
Figure 4. The power spectral density (squared modulus of the Fourier transform) of the X-ray intensity from the primary beam. The peaks at 11.36 Hz and 12.26 Hz correspond to modulation at the rate of fir ng of the gas jets of the attitude control system.